Compositional variations of syntectonic white-mica in low-grade ignimbritic mylonite

G. Arancibia[a,b,*], D. Morata[b]

[a]*Laboratorio Geológico, Servicio Nacional de Geología y Minería, Til-Til 1993, Ñuñoa, Santiago, Chile*
[b]*Departamento de Geología, Universidad de Chile, Plaza Ercilla 803, Santiago, Chile*

Abstract

The Silla del Gobernador Shear Zone (SGSZ), Coastal Range of central Chile (32°S), is a low-grade mylonite generated from a Triassic acidic ignimbritic protolith. Different microstructures (e.g. quarter mats and pressure shadow structures) associated with pressure solution and solution transfer processes and well-preserved porphyroclasts can be observed. White-mica generation appears to be favoured by reaction-softening from dissolved quartz and feldspar porphyroclasts. According to the mylonite fabrics three different types of white-mica can be established (A, B and C) representing mylonites with evidences of relatively low, intermediate and high strain conditions. Deformation mechanisms suggest low-grade (350–400 °C) conditions for mylonitic deformation in the presence of fluids, consistent with the temperature estimations based on chlorite chemistry. The geological setting of the SGSZ also suggests low-pressure ($<$3 kbar) conditions. No major element mobility with respect to protolith composition was observed in low-strained mylonites, whereas for the highly strained mylonites, a marked K_2O secondary input and higher fO_2 conditions during deformation are suggested. The chemical composition of the neoformed white-mica correlates with strain intensity: the high-strained mylonites contain phengitic–celadonitic micas, whereas low-strained mylonites have paragonitic and muscovitic micas. White-mica geobarometry in highly deformed rocks yields pressure values with no geological significance, because the metasomatic K-input favour their high K content, independent of the confining pressure. Thus, the white-mica composition in the mylonites of the SGSZ is controlled by the whole-rock geochemistry and is related to strain conditions.
© 2005 Elsevier Ltd. All rights reserved.

Keywords: White-mica composition; Mylonite; Strain; Whole-rock geochemistry; Coastal Range; Central Chile

1. Introduction

Low-grade volcanic mylonites are characterized by microstructures which evidence heterogeneous strain (Leat and Schmincke, 1993; Williams and Burr, 1994; Conti et al., 1998; Van Staal et al., 2001), for example the development of quarter mat and pressure shadow structures (e.g. Hanmer and Passchier, 1991). These structures are interpreted as the product of pressure solution and solution transfer processes, typical of low-grade metamorphism in the presence of fluids, which can catalyse reaction-enhanced softening involving the production of phyllosilicates (White and

Knipe, 1978; Mitra, 1984; White et al., 1980; O'Hara, 1988; Evans, 1990; Wintsch et al., 1995; Wibberley, 1999).

In the case of low-grade felsic mylonites generated from an ignimbritic protolith, the neoformed metamorphic mineralogy is restricted and mainly characterized by white-mica, feldspar, chlorite and quartz growing in the matrix or pressure-shadows as well as in quarter mat structures (e.g. Williams and Burr, 1994). If we consider that white-mica composition depends mainly on whole-rock chemistry, mineralogical assemblages and pressure–temperature conditions (e.g. Sassie and Scolari, 1974; Guidotti, 1984; Massonne and Schreyer, 1987; Guidotti and Sassi, 1998), the chemistry of the neoformed mica should be relatively homogeneous in low-grade mylonites generated under similar deformation conditions and protolith composition. In this study, we examined the compositional variations of neoformed white-mica product of mylonitic deformation in low-grade mylonites of the Silla del Gobernador Shear Zone, generated under similar

---

* Corresponding author. Address: Laboratorio Geológico, Servicio Nacional de Geología y Minería, Til-Til 1993, Ñuñoa, Santiago, Chile.
   E-mail address: garancibia@sernageomin.cl (G. Arancibia).

deformation conditions, but showing different strain micro-structures and slight differences in whole-rock geochemistry. The aim of this study is to enhance our understanding of the neoformation and/or recrystallization processes of white-mica under different strain conditions. We propose that the mica composition is related not only to the *P–T* conditions and bulk rock composition, but also to the microstructure development in high-strain heterogeneous rocks.

2. Geological setting

The Silla del Gobernador Fault Zone (SGFZ) is a 50-km-long heterogeneous cataclastic–mylonitic belt (Fig. 1) in the coastal region of central Chile (Charrier et al., 1991; Arancibia, 2002, 2004). The mylonite protolith is associated with a Triassic to Lower Jurassic felsic volcano-sedimentary succession and Middle Jurassic intrusive rocks in the Coastal Range of central Chile at 32°S. The acidic tuffaceous rocks contain lithics and phenocrysts of plagioclase and quartz in a vitreous clay matrix with an isotropic fabric. Disseminated chlorite, epidote, calcite and opaque minerals in the matrix are produced by very low-grade metamorphism associated with burial subsidence (Morata et al., 2000). The ignimbritic mylonites contain few deformed porphyroclasts of feldspar, quartz and lithics, in a very fine grained ($<10\ \mu m$) well-foliated, muscovite–chlorite, quartz and feldspar matrix. Heterogeneous deformation with marked fabric changes at the scale of a few metres in the same outcrop is observed throughout the SGSZ. This permits the sampling of various fabric types representative of the mylonites developed within the same ignimbritic protolith.

The SGSZ consists of two distinct sets of structures: (1) NS-striking phyllosilicate-rich mylonite belts with east-dipping foliation, subvertical mineral/stretching lineation and reverse-slip kinematic indicators, and (2) NE-striking cataclastic belts with subvertical foliation and oblique lineation (striae) with dextral-reverse and reverse-dextral kinematic indicators. The geometry and kinematics of both the mylonitic and cataclastic rocks are consistent with a compressional regime with a small dextral component (Arancibia, 2004). Based on structural data, the mylonites and cataclasites are considered to belong to the same ENE-striking regional shear zone, developed along the western border of the Coastal Range of central Chile (Arancibia, 2004). UVLAMP high-resolution laserprobe $^{40}Ar/^{39}Ar$ dating of white-mica formed during mylonitic deformation of the ignimbritic rocks and $^{40}Ar/^{39}Ar$ step heating of biotite from a mylonitized granodiorite suggest that the reverse ductile shearing in the SGSZ was active at around 100 Ma (Arancibia, 2004). The Mid-Cretaceous SGSZ genesis has been associated with crustal shortening and uplift of the Coastal Range (Arancibia, 2004).

3. Analytical methods

Optical microscope and back-scattered scanning electron microscope images from oriented sections parallel to the lineation and perpendicular to the foliation were used for the location, selection and microstructural analysis of white-mica. X-ray diffraction (XRD) analysis of samples was performed in a Siemens 5000 diffractometer, with Cu-Kα radiation and a graphite monochromator, operated at 40 mA and 40 kV, employing a 0.01° step size and 1 s counting time. The X-ray patterns were obtained from powders, as well as oriented and ethylene-glycol treated samples. The whole-rock composition was determined in a Perkin Elmer P430 inductively coupled plasma atomic emission spectrometer (ICP-AES). Detection limits are 0.1% for major elements, 2 ppm for Th and Nb, 1 ppm for Ba, Sr, Zr, Y, Cr, V, Ni, Co, Sc, Cu, Zn, Hf, La, Ce, Nd and Sm, 0.1 ppm for Eu, Gd, Dy, Ho, Er and Yb, and 0.05 ppm for Lu. The standards used were basalt BCR-2, andesite AGV-2 and granite G-2 from the USGS reference materials. Mica chemistry was determined by electron microprobe (EMPA) and energy-dispersive X-ray (EDX) spectrometric analyses by SEM on polished and carbon-coated thin sections. For EMPA a JEOL JXA-8600M (with a spot size of 5 μm, voltage acceleration of 5 KeV, current of 20 nA) and a Cameca SX-50 (with a voltage acceleration of 20 KeV, a spot size of 3 μm and a current of 20 nA) were used. Natural and synthetic minerals were used for standardization. The raw data were corrected by a ZAF procedure. For EDX analysis, a Philips XL30 SEM (with operating software version 5.0, upgraded to version 5.39, 20 keV energy and a spot size of 5.5 μm) was used. Selected white-micas from the quarter mat structures were glued onto Cu grids with a single central hole of 200–400 μm in diameter and thinned by argon ion mill (Gatan Dual Ion Milling 600) and carbon coated. A Philips CM-20 high-resolution transmission electron microscope (HR-TEM), operating at 200 kV with a LaB$_6$ filament and a point-to-point resolution of 2.7 Å, was used. Electron diffraction patterns from selected areas (SAED) and high-resolution lattice-fringe images were thus obtained.

4. Microstructure of the low-grade ignimbritic mylonites

4.1. Microstructure

The ignimbritic mylonitic rocks contain lithic, quartz and feldspar porphyroclasts, 1–10 mm in size, immersed in a very fine grained ($<10\ \mu m$) well-foliated mica-chlorite, quartz and feldspar matrix with scarce epidote and iron oxide crystals (Arancibia, 2004) (Fig. 2a). The strong preferential orientation of the phyllosilicates in the matrix defines the main foliation (Fig. 2b), which is homogeneous and wraps around porphyroclasts. Some mylonites have a shear band secondary foliation cutting the main mylonitic
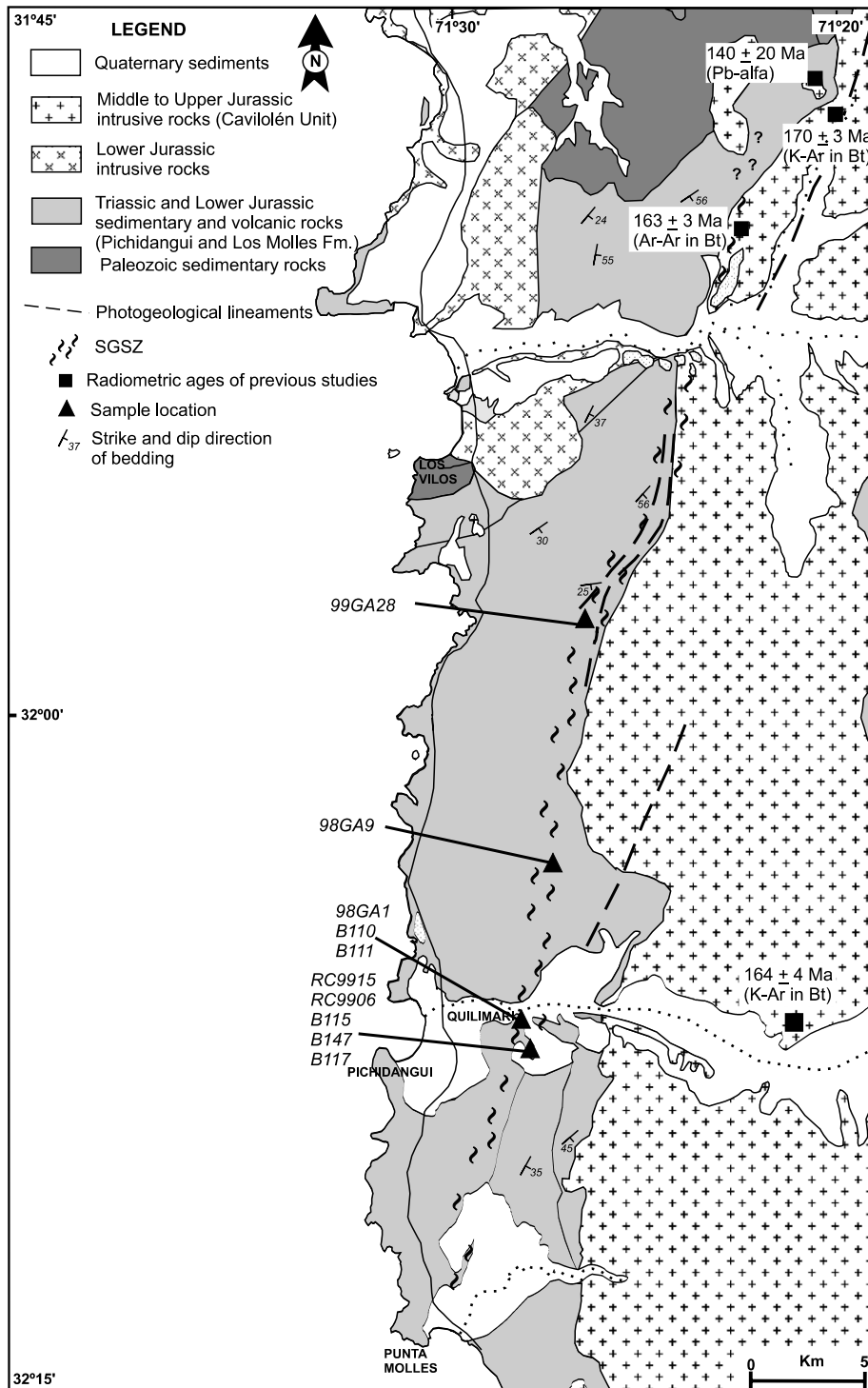
Fig. 1. Regional map (modified from Arancibia (2004)) of the Silla del Gobernador Shear Zone (SGSZ) in the Coastal Range of central Chile (32° Lat. S.) showing the major geological units and structures as well as the location of samples selected for this study.

foliation. They are usually anastomosing, short and wavy, defining the C-type and C′-type shear band cleavage described in Passchier and Trouw (1996), or the C and C′ bands described in Berthé et al. (1979). The C′-type also corresponds to the extensional crenulation cleavage as indicated by Platt and Vissers (1980).

The intracrystalline deformation in most of the quartz, plagioclase and K-feldspar porphyroclasts is manifested mainly by slightly to strongly fractured crystals, although many are undeformed. Some quartz porphyroclasts have elliptical cross-sections, and exhibit undulose extinction and deformation lamellae with a high optical relief, which have

Fig. 2. Microstructure developed in mylonites of the SGSZ. White bar is 0.5 mm long, except for (b). (a) Rounded quartz porphyroclasts with white-mica quarter mats (Qm) and chlorite–quartz strain shadows (Ss) in a fine-grained matrix. Asymmetrical quarter structures indicate sinistral shear. (b) Back-sc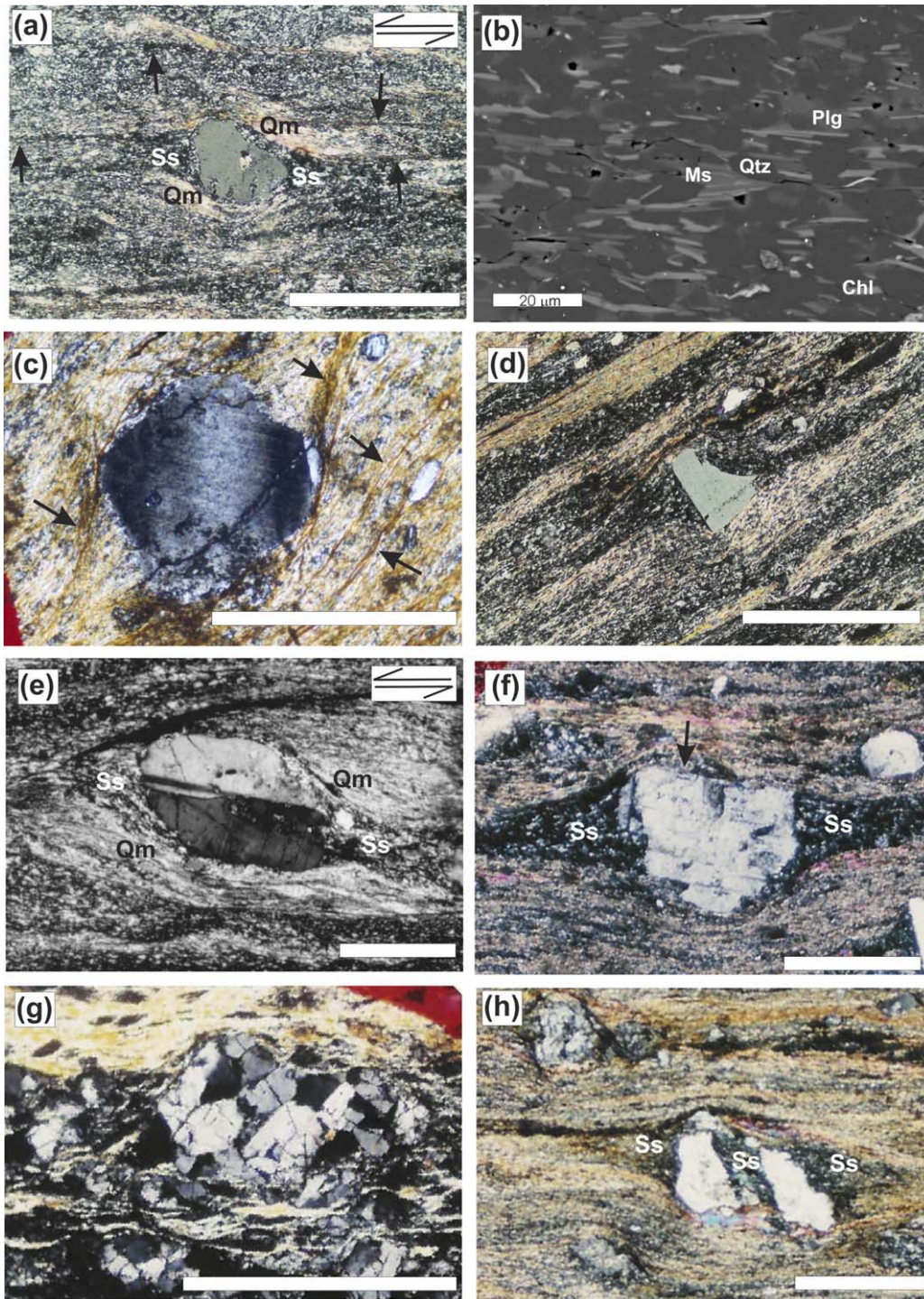attered electron image from scanning electron microscope, showing a very fine-grained well-oriented matrix composed mainly of white-mica (Ms), chlorite (Chl), quartz (Qtz) and plagioclase (Plg). (c) Quartz porphyroclasts with undulose extinction and deformation lamellae. Dark parallel-foliation seams (oblique to microphotograph) consist of insoluble material (mica and opaque minerals) that became concentrated during the dissolution process. (d) Quartz porphyroclast with a curved embayment attributed to dissolution during ductile deformation. No evidence of internal strain is observed. The matrix displays phyllosilicates-rich-bands intercalated with quartz feldspathic-rich zones. (e) Rounded plagioclase porphyroclast attributed to dissolution during deformation. Around the clast asymmetrical quarter mart (Qm) and strain shadow (Ss) structures are well developed, indicating sinistral shear. No evidence of internal strain is observed. (f) Truncated plagioclase porphyroclast associated with strain shadow (Ss) development. (g) Strongly fractured and rotated K-feldspar porphyroclasts in a white-mica-rich matrix. Fragments exhibit undulose extinction. (h) Quartz–chlorite strain shadows (Ss) filling open voids produced by fracturing in quartz porphyroclast.

a distinct preferred orientation (Fig. 2c). Others are anhedral to euhedral with little or no evidence of internal strain (Fig. 2a). Most of the porphyroclasts without internal deformation show embayment microstructures (Fig. 2d). Fractures in quartz contain fine recrystallized quartz grains that are distinct within the otherwise low-strain cores of porphyroclasts. This recrystallization may reflect higher strain concentrated near fractures or may simply represent coarsening and healing of cataclastic material associated with fractures. The plagioclase porphyroclasts ($Ab_{75–100}$, Table 1) tend to be angular or rounded in shape, with evidence of fracturing and slipping on crystallographic cleavage planes, or without any deformational microstructure (Fig. 2e and f). Some plagioclase porphyroclasts show undulose extinction and exhibit deformation twins that taper towards the crystal centre and are restricted to certain parts of the crystal. K-feldspar porphyroclasts can be strongly fractured; undulose extinction is only observed in small fragmented grains (Fig. 2g).

The characteristic microstructure in the SGSZ mylonites is the development of oriented chlorite–quartz and white-mica aggregates around the porphyroclasts, the crystals of which are greater in size (up to 50 μm) than those developed in the rest of the matrix. When chlorite foliation in these aggregates is close to a porphyroclast, an angle with respect to the matrix foliation is observed, whereas away from the porphyroclast, the foliation increases in intensity and curves progressively into the matrix orientation. Strongly foliated mica-rich domains occur in most porphyroclasts, in opposite quadrants with respect to chlorite–quartz domains and are oriented parallel to the main foliation, wrapping the porphyroclasts. The individual mica and chlorite grains show no evidence of intracrystalline deformation such as fractures, folds, kink bands or recrystallized subgrains, although evidence for grain boundary sliding processes in these fine-grained phyllosilicates cannot be observed at the SEM scale. These structures are commonly interpreted as chlorite–quartz strain shadows and mica-rich quarter structures, and their shape can be used as a tool to determine the shear sense (e.g. Hanmer and Passchier, 1991). In the SGSZ, most of the pressure-shadows are symmetrical with respect to the porphyroclast, but some of them are slightly asymmetrical with a sigma geometry (according to the nomenclature of Passchier and Simpson (1986)) and document reverse movement (Fig. 2a and e). This is consistent with other mesoscopic and microscopic kinematic indicators along the SGSZ (Arancibia, 2004). Some strain shadows are developed in open voids between fractured porphyroclasts (Fig. 2h).

According to the intracrystalline deformation developed in the porphyroclasts and foliation structures in the matrix of the SGFZ mylonites from the ignimbritic protolith (Fig. 3a), three different fabrics have been defined (Arancibia, 2002). These three types represent a relative increase of strain and white-mica content in the mylonites of the SGSZ,

independent of the ductile deformation temperature conditions.

Type A is a low-strain fabric (Fig. 3b), typically characterized by the incipient development of chlorite, quartz and plagioclase in pressure-shadows ($Ab_{100–70}$, Table 1) and muscovite quarter mats around the porphyroclasts. The matrix consists of mica, chlorite (Table 2), quartz and feldspar and the foliation is defined by the preferred alignment of very fine grained mica and chlorite (<10 μm). Most porphyroclasts of quartz and plagioclase ($Ab_{80–70}$) have angular shapes and they are preserved intact or slightly fractured.

Type B is the intermediate-strain fabric (Fig. 3c), which is similar to previously described mylonites, but quarter mat and strain shadow structures are well developed and the phyllosilicate content is higher. Pressure-shadows contain mainly chlorite (30–50 μm in size, Table 2) and quartz (10–20 μm in size), whereas quarter mat structures are formed exclusively by mica up to a grain size of 50 μm. Additionally, mica is developed in other structures such as strain caps and shear bands. Quartz porphyroclasts display embayment shapes and some are fractured, with deformation lamellae and local fine-grained crystals in fractures and along grain boundaries. Rounded plagioclase porphyroclasts ($Ab_{85–75}$, Table 1) can be fractured and may present undulose extinction. Most of them are unaltered, some slightly sericitized.

Type C is the higher strain fabric (Fig. 3d), the foliation of which, defined by oriented muscovite–chlorite and quartz, K-feldspar and opaque mineral aggregates, is affected by extensional crenulation cleavage and conjugate shear bands (c.f. Passchier and Trouw, 1996) of muscovite, vermiculite and biotite (Table 2). Quarter mats and strain shadows are weakly developed. Albite porphyroclasts (Ab_{98}, Table 1) are strongly fractured and some display tapering deformation twins ($Ab_{100–96}$, Table 1) and undulose extinction. K-feldspar porphyroclasts are relatively more abundant than in the A and B types and are strongly fractured and rotated. Quartz porphyroclasts exhibit undulose extinction, deformation lamellae and recrystallized subgrains in fractures. With respect to the other two fabrics, the mica content is the highest. Abundant iron oxide crystals (0.05–0.1 mm) are disseminated in the matrix, following the main foliation.

The main microstructural characteristics and metamorphic mineralogical assemblages of these three types, defined by minerals in structures such as pressure-shadows, quarter mats, foliation and shear bands are summarized in Table 3.

4.2. Deformation mechanisms

In the SGSZ most quartz, plagioclase and K-feldspar porphyroclasts exhibit no evidence of intracrystalline strain. Where porphyroclasts present intracrystalline deformation it is mainly reflected by slight to intense fracturing. Crystal-plastic processes are restricted to occasional undulose

Table 1
Representative EMPA and EDX analyses of feldspars of Type A, B and C mylonites from the SGSZ

Sample	B115	B115	B115	98GA1	98GA1	98GA1	B110	98GA9	98GA9	99GA28A	99GA28A
Domain	ss	f	p	p	p	m	f	dt	m	p	dt
Type	A	A	A	B	B	B	B	C	C	C	C
Analysis	EDX	EDX	EMPA	EMPA	EMPA	EMPA	EMPA	EMPA	EMPA	EMPA	EMPA
SiO_2	62.59	64.10	65.17	62.53	64.81	59.57	61.46	67.92	63.44	65.90	65.93
TiO_2	0.04	0.03	0.01	0.00	0.02	0.00	0.01	0.04	0.41	0.00	0.01
Al_2O_3	24.04	22.43	22.63	23.72	21.81	23.90	24.69	19.96	21.63	19.54	19.60
FeO	0.09	0.85	0.20	0.24	0.20	0.27	0.27	0.03	3.48	0.11	0.01
MnO	0.07	0.11	0.00	0.01	0.00	0.00	0.00	0.00	0.01	0.02	0.02
MgO	0.00	0.06	0.00	0.01	0.00	0.02	0.00	0.01	1.61	0.00	0.00
CaO	5.38	2.73	3.81	4.49	2.93	6.26	6.35	0.66	0.06	0.13	0.08
Na_2O	8.17	9.07	9.29	8.52	9.99	7.36	7.97	11.27	0.23	11.44	11.43
K_2O	0.00	0.07	0.07	0.47	0.05	0.07	0.04	0.09	8.10	0.09	0.08
Total	100.39	99.51	101.17	100.00	99.80	97.44	100.78	99.98	98.97	97.22	97.14
Si	2.758	2.839	2.839	2.770	2.861	2.715	2.711	2.971	2.875	2.966	2.967
Ti	0.001	0.001	0.000	0.000	0.001	0.000	0.000	0.001	0.014	0.000	0.000
Al	1.248	1.171	1.162	1.238	1.135	1.284	1.283	1.029	1.156	1.036	1.040
Fe^{2+}	0.003	0.031	0.007	0.009	0.007	0.010	0.010	0.001	0.132	0.004	0.000
Mn^{2+}	0.003	0.004	0.000	0.000	0.000	0.000	0.000	0.000	0.001	0.001	0.001
Mg	0.000	0.004	0.000	0.000	0.000	0.001	0.000	0.001	0.109	0.000	0.000
Ca	0.254	0.130	0.178	0.213	0.138	0.306	0.300	0.031	0.003	0.006	0.004
Na	0.698	0.779	0.784	0.732	0.855	0.650	0.681	0.955	0.020	0.998	0.998
K	0.000	0.004	0.004	0.027	0.003	0.004	0.002	0.005	0.468	0.005	0.005
Σ cations	4.966	4.965	4.974	4.990	5.000	4.970	4.989	4.994	4.777	5.017	5.014
%An	26.68	14.20	18.39	21.94	13.90	31.85	30.49	3.10	0.56	0.60	0.38
%Ab	73.32	85.37	81.20	75.33	85.79	67.73	69.26	96.37	4.13	98.90	99.16
%Or	0.00	0.43	0.41	2.73	0.31	0.42	0.25	0.53	95.31	0.50	0.46

The structural formulae was calculated on the basis of eight oxygens. Total Fe was calculated as FeO. ss, strain shadow; f, filling fractures; m, matrix; dt, deformation twins; p, relic porphyroclast.
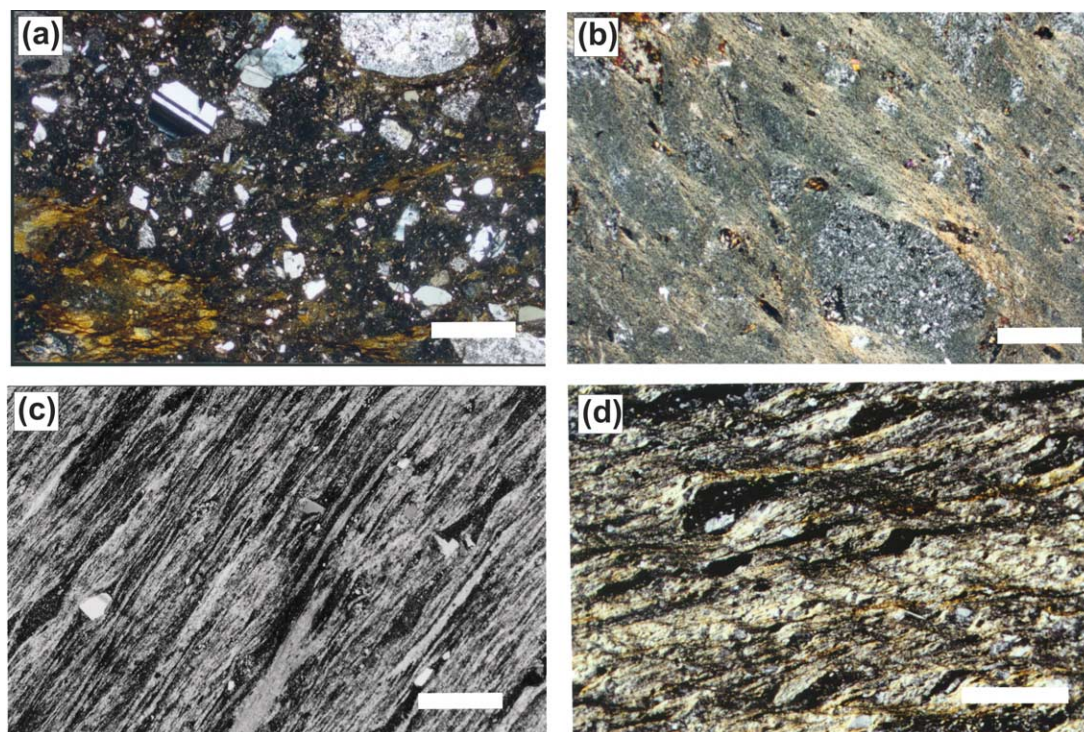
Fig. 3. Photomicrographs (crossed nichols) of the different fabric types defined in the SGSZ mylonites. White bar is 1 mm long. (a) Undeformed acid ignimbrite (=protolith) from the Triassic Pichidangui Formation. (b) Relatively low-strained mylonite, representative of Type A, with an incipiently foliated, matrix poor in micas (sample B-147). (c) Moderately strained mylonite, representative of Type B, with strongly foliated mica-rich matrix (sample B110). (c) Highly-strained mylonite, representative of Type C, with strongly foliated and crenulated mica-rich matrix (sample 98GA9).

extinction and deformation lamellae in quartz porphyro-clasts, as well as tapering deformation twins and undulose extinction in strongly fractured plagioclase and K-feldspar porphyroclasts.

According to the crystal size of the adjacent protolith, we conclude that grain-size reduction of quartz and feldspar is important. However, feldspar and quartz did not become fine-grained by repeated fracturing, i.e. by cataclasis, alone, because the bimodal grain-size distribution does not reflect characteristic wide grain-size range of cataclasis (e.g. Fitz Gerald and Stünitz, 1993). Concomitant mineral precipi-tation from fluids is evident, because voids created between or around porphyroclasts are filled with material precipi-tated from solution (Fig. 2h). Dissolution processes occurred at grain boundary and fractures, because the rounded shape of the feldspar (Fig. 2e) and embayment of quartz (Fig. 2d) cannot be attributed to dynamic recrystalli-zation (Tullis and Yund, 1985). Truncated shapes in undeformed feldspar porphyroclasts can be the result of dissolution mechanisms similar to those described by Hippertt (1994), but without important crystal plasticity (Fig. 2f). Finally, well-developed strain shadows and quarter mat structures suggest that pressure solution and solution transfer were important deformation mechanisms (e.g. Hanmer and Passchier, 1991).

Pressure solution and solution transfer of material are dominant under low-grade metamorphic conditions where

fluids are abundant and where deformation mechanisms favoured at higher temperatures, such as intracrystalline deformation, are uncommon. Selective pressure solution at grain contacts occurs because the solubility of a mineral in an aqueous fluid is higher where a crystal lattice is under high stress than at localities where stress is relatively low (e.g. Knipe, 1989). The dissolved material can diffuse away from the sites of high solubility down a stress-induced chemical potential gradient to nearby sites of low-solubility stress by stress-induced solution transfer. The deposition of material from solution may occur at adjacent free grain boundaries or over a large distance as veins or strain shadows and its composition can be different from the consumed minerals (Rutter, 1983). Microstructural evi-dence in support of a pressure solution mechanism in the SGSZ includes the abundant anastomosing mica folia or opaque residues separating domains of augen-shaped quartz and feldspar (e.g. Wintsch, 1978) (Fig. 2c). Moreover, pressure solution may be inferred to have occurred because there is evidence of mineralogical redistribution arranged systematically around mechanical heterogeneities in the rock, such as the migration of more soluble material from sites of stressed objects (porphyroclasts) facing principal load directions, to the strain shadow areas (Rutter, 1983) (Fig. 2f). The deposition of material from solution is evidenced by new grains or fibrous overgrowth of grains within the strain shadows (Fig. 4). New grains grown from

Table 2
Representative EMPA and EDX analyses of mafic phyllosilicates of Type A, B and C mylonites from the SGSZ

Sample	B115	B115	B115	98GA1	98GA1	98GA1	98GA9	99GA28A	98GA9	98GA9
Domain	ss	ss	ss	ss	ss	m	m	m	m	qm
Type	A	A	A	B	B	B	C	C	C	C
Analyses	EDX	EDX	EDX	EMPA	EMPA	EMPA	EDX	EMPA	EDX	EDX
Mineral	Chl	Chl	Chl	Chl	Chl	Chl	Verm/Bt	Verm/Bt	Bt	Bt
SiO_2	24.76	23.45	23.48	25.25	24.85	25.97	43.93	42.21	43.74	43.63
TiO_2	0.05	0.12	0.06	0.03	0.05	0.05	0.04	0.11	1.34	1.19
Al_2O_3	23.96	22.7	23.41	22.96	22.80	23.69	20.44	18.89	18.87	19.18
FeO	31.35	30.62	31.28	20.96	21.68	20.87	14.68	14.17	12.44	14.48
MnO	0.05	0.09	0.00	0.40	0.35	0.41	0.03	0.10	0.05	0.02
MgO	8.85	8.57	8.57	13.89	15.65	15.61	4.78	6.69	7.96	8.23
CaO	0.03	0.04	0.08	0.19	0.10	0.15	0.62	0.30	0.07	0.11
Na_2O	0.00	0.05	0.00	0.06	0.06	0.03	0.55	0.11	0.33	0.24
K_2O	0.04	0.12	0.00	0.01	0.00	0.02	2.00	6.77	8.31	6.00
Total	89.19	85.76	86.95	83.75	85.53	86.81	87.10	89.33	93.11	93.08
N Ox	28	28	28	28	28	28	22	22	22	22
Si	5.269	5.218	5.155	5.439	5.271	5.379	6.620	6.421	6.379	6.334
Al^{iv}	2.731	2.782	2.845	2.561	2.729	2.621	1.380	1.579	1.621	1.666
Al^{vi}	3.278	3.171	3.212	3.269	2.971	3.162	2.250	1.808	1.622	1.616
Ti	0.008	0.020	0.010	0.005	0.007	0.008	0.005	0.013	0.147	0.130
Fe^{2+}	5.579	5.698	5.743	3.776	3.846	3.615	1.850	1.802	1.517	1.758
Mn^{2+}	0.009	0.017	0.000	0.074	0.064	0.071	0.004	0.013	0.006	0.002
Mg	2.807	2.843	2.805	4.459	4.948	4.821	1.074	1.516	1.730	1.781
Ca	0.007	0.010	0.019	0.044	0.022	0.034	0.100	0.048	0.011	0.017
Na	0.000	0.022	0.000	0.025	0.026	0.012	0.161	0.032	0.093	0.068
K	0.011	0.034	0.000	0.003	0.001	0.006	0.384	1.314	1.546	1.111
Σ cations	19.716	19.813	19.801	19.655	19.885	19.731	13.831	14.546	14.673	14.484

The structural formulae was calculated on the basis of 28 oxygens for chlorite (Chl) and 22 oxygens for vermiculte/biotite (Vrm/Bt) and biotite (Bt). Total Fe was calculated as FeO. ss, strain shadow; qm, quarter mats; m, matrix.

Table 3
Summary of mineralogy and microstructure of Type A, B and C mylonites from the SGSZ

Characteristics	Microstructural types		
	Type A	Type B	Type C
Relative strain	Low	Intermediate	High
Sample	B115, B147	B111, B110, 98GA1	98GA9, 98GA28
Mineralogy	Modal proportion		
Quartz	4	4	3
Plagioclase	2 (Ab_{60-85})	1 (Ab_{60-85})	1 (Ab_{95-100})
K-feldspar	0	0	1 (Microcline)
White-mica	1 (Ms–Pg)	1 (Ms)	1 (Ms–Phe)
Chlorite	1	1	0
Chlorite/vermiculite	1	0	0
Vermiculite/biotite	0	0	1
Biotite	0	0	1
Fe–Ti oxides (Il, TiMgt, Mgt, Rutile)	1	1	1

Notes: 4=60–80%; 3=40–60%; 2=20–40%; 1=5–20%; 0=<5%. Muscovite (Ms) corresponds to the 2M1 politype

Structures	Relative development		
In the matrix (<50 μm)			
Foliation (S)	xxx	xxx	xxx
Shear bands (type C′)	no	xx	xxx
Pressure-shadows	x	xx	x
Strain caps	x	xx	no
Quarter mats	xx	xx	x
In porphyroclasts (>0.5 mm)			
Quartz			
Fracture	x	x	xxx
Undulose extinction	no	x	xx
Deformation lamellae	no	x	xx
Recrystallized grains in boundaries and fractures	no	x	xx
Plagioclase			
Fracture	x	x	xxx
Undulose extinction	no	x	xx
Deformation twins	no	no	xx
Recrystallized grains in boundaries and fractures	no	x	x
K-feldspar (only in type C)			
Fracture	–	–	xx
Undulose extinction	–	–	x

Notes: no, absent; x, slight; xx, intermediate; xxx, high

Mineralogical abundance is estimated qualitatively from DRX patterns and petrographic study. The plagioclase composition was determined from EMPA.

solution may be recognized by a lack of intracrystalline deformation structures and well-defined crystal faces. Strain shadows, strain fringes, overgrowths and intragranular fractures are possible local precipitation sites for some of the dissolved materials. Strain shadows in the SGSZ mylonites are commonly enriched in soluble minerals such as quartz and chlorite, whereas strain caps and quarter mat domains are enriched in insoluble minerals such as micas and opaques (Fig. 4). In all cases, strain shadows are disposed in opposite quadrants of quarter mats, as a mineralogical distribution geometrically consistent with overall strain in the shear zone. The local scale of these processes suggests that earlier fine-grained minerals of mica–chlorite–feldspar–quartz composition were present in the matrix adjacent to the porphyroclasts. In this case, pressure solution at the site of strain caps or quarter mats, solution transfer and redeposition of material at grain boundaries in the developing strain shadow are envisaged for these microstructures.

Brittle fracturing and limited crystal-plastic deformation of quartz, accompanied by simultaneous considerable fluid material distribution and deposition, occur commonly at very low-grade conditions (below 300 °C) (e.g. Rutter, 1983; Groshong, 1988; Knipe, 1989; Fitz Gerald and Stünitz, 1993). However, deformation lamellae in quartz become important at low-grade conditions (300–400 °C). In this range feldspar still deforms mainly by internal microfracturing accompanied by minor dislocation gliding, so that tapering deformation twins and undulose extinction can be present (e.g. Pryer, 1993). Temperature estimations for SGSZ mylonites, based on the Cathelineau (1988) chlorite geothermometer, indicate values in the range of 320–380 °C for Type A and B mylonites (Arancibia, 2002). The presence of biotite crystals together with vermiculite/
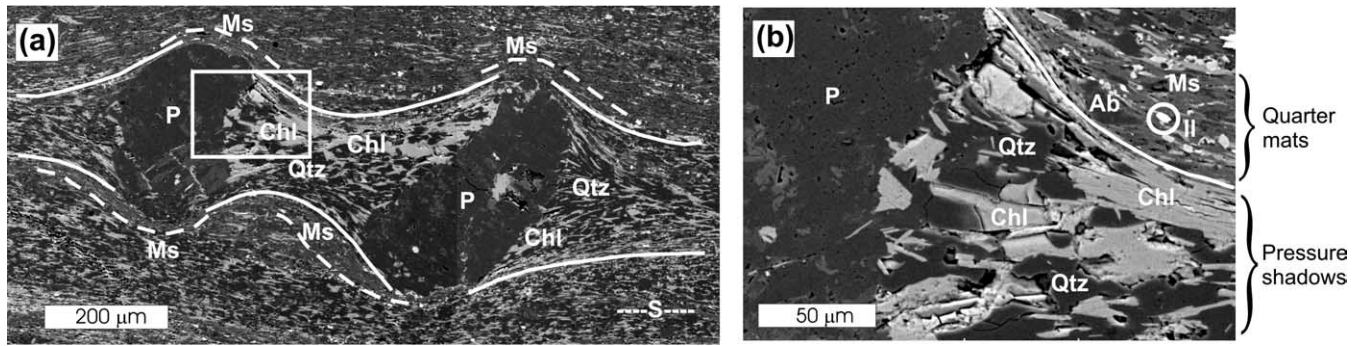
Fig. 4. (a) Scanning electron microscope image of pressure shadow (continuous line) and quarter mat (dotted line) structures around a porphyroclast (P) in a low-grade volcanic mylonite of the SGSZ. (b) Detail of the microstructure. Mineral abbreviations: Ab = albite, Chl = chlorite, Il = ilmenite; Ms = muscovite; Qtz = quartz.

biotite intergrown in Type C mylonites (Table 2) suggests temperature conditions above 300–400 °C (Spear, 1993), as proposed by Velde (1978) and Ruiz-Cruz (1999) for the transition interval vermiculite/biotite. The neoformed minerals overprinted on the igneous protolith are white-mica, quartz, chlorite, albite ± vermiculite ± biotite and minor amounts of opaque minerals. This paragenesis is consistent with the upper limit of the green schist metamorphic facies as also indicated by the microstructure. These constraints suggest that deformation in the SGZS occurred at temperatures between 350 and 400 °C in the presence of a fluid phase.
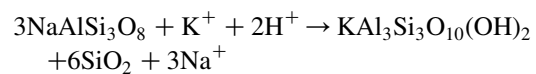
The absence of phyllosilicates in the adjacent undeformed protolith, its development in the well-foliated matrix and well-developed quarter mat-strain shadow structures, indicate that most phyllosilicates were generated during deformation. In fact, these last two structures are not present in undeformed ignimbritic rocks (Williams and Burr, 1994). Exceptionally, limited intracrystalline deformation of quartz and feldspar at these temperatures has been documented in previous studies of low-grade deformed ignimbrites (Williams and Burr, 1994). This phenomenon appears to be associated with the previously discussed pressure solution and solution transfer mechanisms and a dominantly syntectonic phyllosilicate generation. The syntectonic generation of phyllosilicates in low-grade fault rocks has been well documented in quartz-feldspathic fault zones and is known as *reaction-enhanced softening* or *reaction softening* (e.g. White and Knipe, 1978; Mitra, 1984; White et al., 1980; O'Hara, 1988; Evans, 1990; Wintsch et al., 1995). This process involves the breakdown of relatively strong feldspars to easily deformable phyllosilicates producing a reaction-softening effect on faulted rocks.

4.2.1. Phyllosilicate generation and reaction softening

Fluid flow through fault zones may cause phyllosilicates to become concentrated in high-strain fault zones at the expense of more soluble minerals, in this way bringing fault strength closer to the intrinsic strength of phyllosilicates with increasing strain (Bos and Spiers, 2001). Reaction

softening corresponds to the mineralogical replacement of stronger framework and chain silicates (e.g. quartz and feldspars) by phyllosilicates, with strain accommodation in the resulting foliated rock by dislocation gliding and grain boundary sliding generating a reaction weakening. Strong preferred orientations of phyllosilicates may develop by mechanical and chemical processes and phyllosilicate grains oriented by shearing on (001) planes are very weak by comparison with other minerals (Wintsch, 1978; Shea and Kronenberg, 1992).

Under low-grade conditions, the weakest phase will usually be mica (Shea and Kronenberg, 1992). If large amounts of water are introduced into the quartz-feldspathic system, feldspar must dissolve and muscovite would precipitate, as the solutions approach chemical equilibrium with the initial mineral assemblage (Qtz–KFd–Plg). Considering the protolith mineralogy and the inferred conditions at which deformation took place in the SGSZ, the earliest development of muscovite most likely proceeded through the breakdown of the alkali feldspars according to the following softening reactions (Wibberley, 1999):

$$3NaAlSi_3O_8 + K^+ + 2H^+ \rightarrow KAl_3Si_3O_{10}(OH)_2 + 6SiO_2 + 3Na^+$$

Albite → muscovite + silica

$$3KAlSi_3O_8 + 2H^+ \rightarrow KAl_3Si_3O_{10}(OH)_2 + 6SiO_2 + 2K^+$$
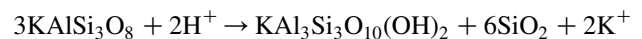
Orthoclase → muscovite + silica

In both equations, an acid fluid is invoked. A reasonable proposition is that silica released by orthoclase and albite muscovitisation during phyllosilicate generation migrated locally and reprecipitated in voids created as strain shadows and fractures in the porphyroclasts (Wibberley, 1999). The addition of MgO to the system may add chlorite and biotite to the mineral assemblage (Wintsch et al., 1995).

The dissolution of quartz and feldspar will increase the activities of the alkalis, aluminium, and silica in the adjacent aqueous solutions. Fracturing of quartz and feldspar porphyroclasts permits surface reaction and granular sliding

which increase the permeability (Wibberley, 1999). The mica that will precipitate from solutions of this composition will be muscovite and its (001) plane will be oriented normal to λ_3 (Tullis and Wood, 1975). As pressure solution of the quartz and feldspar continues, the porosity will be reduced, and all the minerals will experience higher stresses and begin to dissolve. When this occurs, the earlier-formed muscovite and chlorite will begin to recrystallize (probably by a dissolution–precipitation mechanism) with their (001) planes oriented normal to λ_3. Thus, the first phyllosilicates to crystallize along the foliation will be muscovite and chlorite formed from pressure solution of quartz and feldspars, followed later, as strain increases and porosity is reduced, by the recrystallization of the earlier-formed phyllosilicates in the matrix. This process has been described by Wintsch (1978) for mediumly metamorphosed sediments.

In the SGSZ, syntectonic phyllosilicate growth associated with reaction softening can be the explanation for the strength of most quartz and feldspar porphyroclasts. The fine-grained matrix can deform by grain boundary sliding, or by pressure solution and precipitation, at such low differential stress that limited intracrystalline deformation is induced in quartz and feldspar porphyroclasts. Additionally the ignimbritic nature of the protolith favours a rheological behaviour in which the porphyroclasts lie isolated (without contacts between them) in a very fine-grained matrix. This clast-matrix rheology (according to the terminology of Handy (1990)) favours the deformation of only the weak mineral(s), whereas the strong mineral(s) remain(s) rheologically passive and concentrate(s) stress and strain in the weak matrix.

5. Geochemistry

5.1. Whole-rock composition

Low-grade metamorphic reactions occur as open systems with respect to some mobile major and trace elements, in different fluid phase compositions. Chemical changes associated with deformation can be studied by mass-balance calculations comparing the geochemistry of the precursor non-deformed (or only slightly deformed) protolith with the mylonites (e.g. Condie and Sinha, 1996; Hippertt, 1998; Bialek, 1999; Zulauf et al., 1999; Wibberley, 1999). In the case of the SGSZ, eight whole-rock geochemical analyses of samples representative of the three defined types are used to check the element mobility compared with two samples of the protolith (Table 4). Additional four samples from Triassic acid volcanic lava flows of the Pichidangui Formation outcropping at the coastline (data from Morata et al. (2000)) are also considered as representative of undeformed protolith. Assuming Zr to be an essentially immobile element, it is possible to check the mobility/immobility of elements using two-element variation

diagrams (Fig. 5a). Those elements showing a good correlation with Zr would thus be considered as essentially immobile, whereas mobile elements would plot outside a theoretical correlation line. Elements plotting above and below this line would be gained or lost by the system, respectively. A good correlation between Zr and Hf (Fig. 5b) confirms the immobility of these trace elements while the variations observed in these incompatible trace elements can be related to the primary igneous differentiation, mostly due to the relative heterogeneity of the ignimbritic and lava flow protolith. Na_2O and CaO present an erratic behaviour due to the mobility of these elements, but higher Na_2O values are observed in mylonites of Type A (see Table 4). SiO_2 and Al_2O_3 plots show scattering (Fig. 5c and d) probably related to the inherent heterogeneity of the ignimbritic mylonite with variable quartz and feldspar abundance, although a relative positive correlation with Al_2O_3 is observed. Larger differences are observed in the K_2O and Fe_2O_3/FeO ratios (Fig. 5e and f), the highest values observed in mylonites of Type C. The K_2O content in mylonites of Type C (5.24–5.41%wt) is also higher than the highest K_2O values of the undeformed Triassic acid lava flow from the Pichidangui Formation (average of 3.32%wt; Morata et al., 2000). Given the tholeiitic affinity of these volcanic rocks (Morata et al., 2000), high K_2O values up to 5%wt can be only explained if a metasomatic secondary input (related to the deformation) is invoked. To explain the high Fe_2O_3/FeO ratio observed in mylonites of Type C, high fO_2 conditions would have prevailed during the low-grade fluid/rock interaction, as evidenced by the rather abundant Fe-oxides.

Rare earth element mobility/immobility can be checked using multi-element diagrams in which the average chemical composition of the three microstructural types are normalized with respect to the average of the protolith analyses (Fig. 6). Light rare earth elements show a rather immobile behaviour, whereas heavy rare earth elements are slightly enriched in mylonite rocks. Eu shows a slight negative anomaly, probably related to the alteration of feldspar during milonitization.

Mass transfer and volume changes during milonitization can be graphically evaluated by the isocon method (Grant, 1986), in which all element concentrations (multiplied by different scaling factors) are plotted on protolith versus altered rocks. Those elements plotting on the same straight line passing through the origin would define an isocon. If no volume change had occurred, this line would have a 1:1 ratio and elements systematically plotting above and below this constant mass isocon would be gained or lost to the system. Those elements with erratic trends (below the isocon in some rocks and above in some others) would have migrated laterally within the system, rather than having been added or removed from it (Hippertt, 1998). Isocon diagrams (Fig. 7) show mass-conservative processes in samples B-117 (mylonite of Type A, Fig. 7a) and B-111

Table 4
Whole-rock element geochemistry (major elements in %wt and trace elements in ppm) from undeformed protolith and mylonites of the three microstructural types defined in the SGSZ

Sample	RC9915	RC9906	B147	B115	B117	B110	B111	98GA1	98GA9	99GA28
Type	Protolith	Protolith	A	A	A	B	B	B	C	C
SiO_2	66.49	69.76	73.85	63.59	75.42	73.87	64.09	73.12	67.74	69.70
TiO_2	1.07	1.45	0.27	1.50	0.20	0.25	1.30	0.26	1.51	0.35
Al_2O_3	15.30	12.32	12.97	19.20	11.64	13.64	16.04	14.84	12.99	14.00
Fe_2O_3	2.55	2.50	1.55	1.42	2.97	0.94	3.03	1.05	6.92	3.83
FeO	3.88	5.04	1.92	3.32	0.84	2.00	3.60	1.76	0.80	0.44
MnO	0.10	0.13	0.03	0.02	0.04	0.04	0.09	0.03	0.01	0.02
MgO	1.84	2.35	1.55	1.21	2.20	1.70	1.80	1.69	0.83	1.20
CaO	0.60	1.12	1.28	1.43	0.60	1.75	1.85	1.03	0.09	0.10
Na_2O	3.26	1.30	1.85	3.07	0.91	1.86	4.31	1.61	1.76	2.55
K_2O	1.71	0.78	2.53	1.34	0.78	1.39	1.03	1.83	5.41	5.24
P_2O_5	0.30	0.12	0.01	0.10	0.01	0.07	0.07	0.04	0.05	0.03
LOI	2.69	3.00	2.04	3.56	4.07	2.07	2.51	2.64	1.81	2.35
Total	99.79	99.87	99.85	99.76	99.68	99.58	99.72	99.90	99.92	99.81
Ba	1100	211	580	600	355	455	150	680	500	1000
Th	7.4	6.8	8.0	9.0	7.8	9.6	5.9	11.0	2.0	11.0
Nb	12	8	11	15	8	13	10	11	5	11
Sr	295	159	390	405	130	240	237	225	80	55
Zr	264	187	384	394	209	284	222	323	165	264
Y	49	35	72	75	42	54	37	57	32	64
Cr	12	11	5	12	7	8	20	7	14	5
V	53	130	19	67	17	11	89	13	177	49
Ni	8	10	7	13	24	4	13	9	11	15
Co	17	15	3	14	5	4	18	6	18	6
Sc	19	21	5	23	4.4	4.9	18	6	21	8
Cu	9	23	8	9	20	10	24	10	11	5
Zn	93	110	103	83	101	66	77	63	73	107
Hf	6.7	4.6	9.9	10.7	5.9	7.7	5.3	10.0	3.8	10.4
La	28	19	39	23	22	26	24	32	19	33
Ce	66	50	92	82	52	60	64	68	47	77
Nd	37	30	46	31	32	33	35	36	28	39
Sm	7.67	6.66	10.27	3.87	6.87	8.09	8.28	8.40	5.43	9.26
Eu	2.12	1.67	1.65	1.54	1.01	1.15	1.85	1.15	1.49	1.47
Gd	8.97	7.00	10.84	8.42	6.80	9.05	8.09	8.69	5.86	9.17
Dy	8.83	7.37	13.00	13.00	7.22	10.52	8.13	10.50	6.26	11.09
Ho	1.78	1.39	2.76	2.94	1.55	2.13	1.53	2.21	1.15	2.55
Er	4.66	3.86	7.80	8.72	4.60	6.04	3.42	6.40	3.23	7.65
Yb	4.80	3.63	7.72	8.63	4.50	5.53	3.39	6.42	3.21	7.73
Lu	0.72	0.57	1.20	1.18	0.70	0.83	0.51	0.98	0.47	1.20

LOI, loss on ignition.
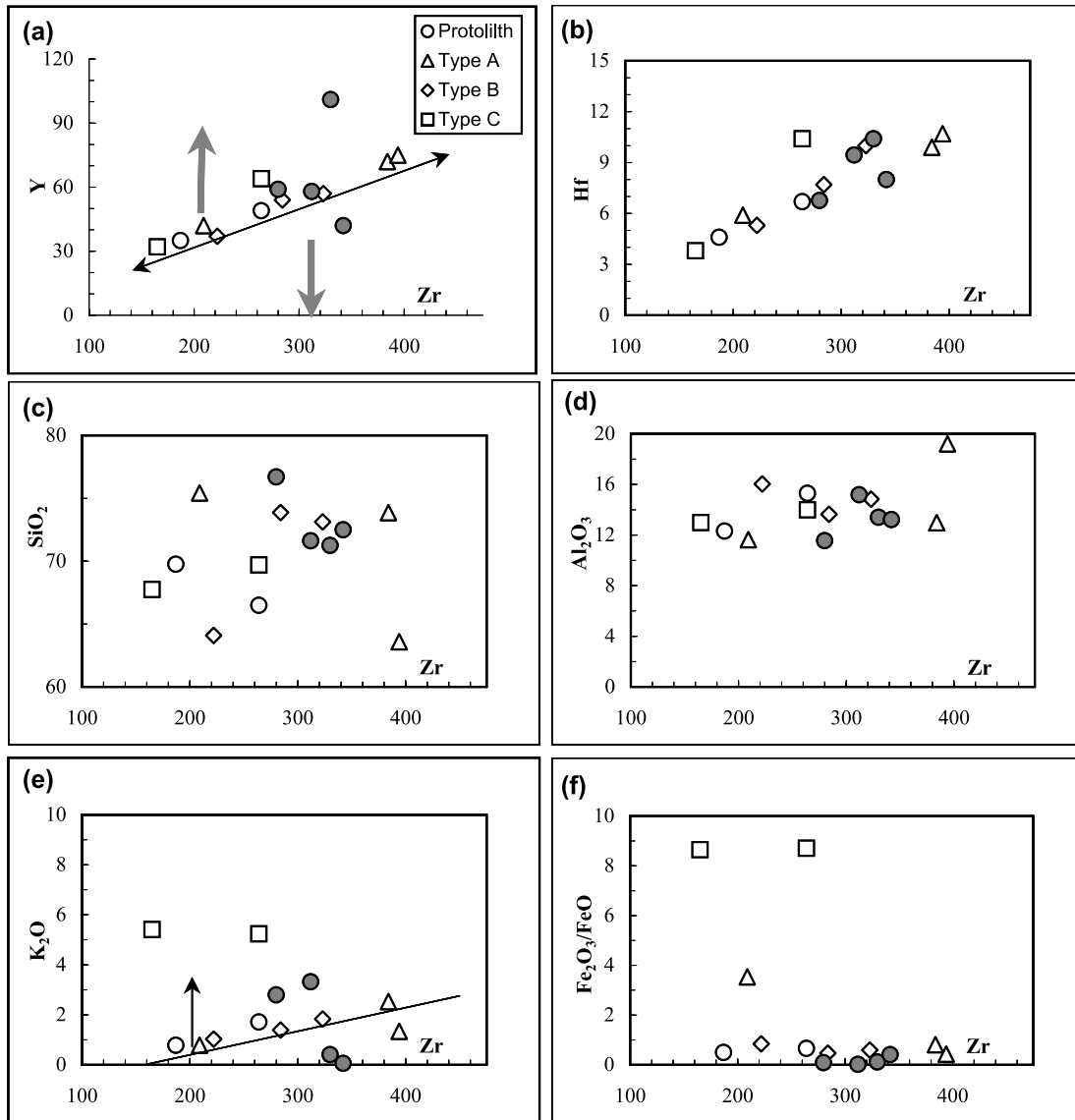
Fig. 5. Variation diagrams of some trace (in ppm) and major (in %wt) elements with respect to Zr for mylonites of the SGSZ. (a) Zr vs Y; (b) Zr vs Hf; (c) Zr vs SiO_2; (d) Zr vs Al_2O_3; (e) Zr vs K_2O; (f) Zr vs Fe_2O_3/FeO. In the Zr vs Y and Zr vs K_2O diagrams, straight line shows the primary variation due to the incompatibility of these elements. The mobility of elements due to deformation is shown by arrows. Additional chemical analyses from undeformed Triassic acid volcanic lava flows (grey circles; data from Morata et al. (2000)) are plotted for comparison.

(mylonite of Type B, Fig. 7c), with almost all immobile elements plotting along the mass-conservative isocon and reflecting erratic behaviour (due to lateral mobility) of most of the mobile elements. Volume loss of around 25% is required for samples B-115 (mylonite of Type A, Fig. 7b) and B-110 (mylonite of Type B, Fig. 7d) in order to trace the isocon based on mostly immobile elements. In these samples, Fe concentrations tend to be lower and Ca to be higher. Na values show an erratic behaviour. Finally, for samples 98GA9 and 99GA28 (mylonites of Type C, Fig. 7e and f), a mass-conservative process can also be assumed if an isocon is fitted for the less mobile elements. A clear input of K^+ and Fe^{3+} and a decrease in Fe^{2+} is observed.
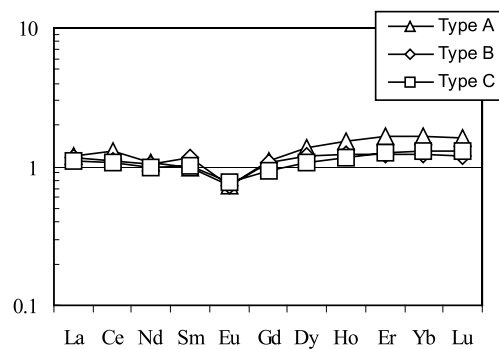
Fig. 6. Rare earth element multi-element normalized diagram of average composition of mylonites from the SGSZ. Normalized values are the average of rare earth elements in the ignimbritic protolith.

5.2. White-mica composition

White-mica from six samples representative of the three defined types (Fig. 1) were analyzed by EMPA and EDX. Despite the small size of the white-mica crystals (normally <50 μm), no significant differences were observed between analyses carried out by EMPA or EDX. The structural formulae were calculated on the basis of 22 oxygens, and, according to the criteria of Guidotti and Sassi (1998), only data with Σoxide >90%, Si content >6.00, Σ(Na+Ca+K) >1.60 and a Ca content <0.1 a.p.f.u. were selected. If white-mica analyses fall below 6.00 Si a.p.f.u., they are most likely of poor quality regardless of the rock type. If the value for (Na+K+Ca) is lower that ca. 1.6, either the

analyses are poor, or the analysed flakes include layers of an alkali-free sheet silicate, or alternatively some other, non-analysed component (such as Ba, Sr, NH_4^+, etc.) is located in the XII sites. Finally, white-mica analyses showing more than 0.01 Ca a.p.f.u. (as commonly seen in wet chemical analyses due to impurities) are certainly to be considered suspect. However, although muscovite (K-bearing white-mica) has very little Ca^{2+} replacing K^+, paragonite (Na-bearing white-mica) can have significant Ca replacing Na (Guidotti and Sassi, 1998). Representative analyses of mica developed in the matrix and in quarter mat structures from the three different defined microstructural types are shown in Table 5.

Muscovite, represented by the formula $K_2Al_4(Al_2Si_6O_{20})$

Fig. 7. Isocon diagrams (constructed with the Gresens 92 code; Potdevin, 1993) of representative samples from the three different mylonite types in the SGSZ with respect to the ignimbritic protolith. In (b) and (d), isocons were plotted assuming a constant volume (solid line) and a volume loss of 25% (dotted line). Scaling factors used to plot elements were 0.1 for Ba and Zr, 0.5 for Sr, 1 for SiO_2, Th, Y, Sc, V, Zn and rare earth elements, 5 for Al_2O_3, Na_2O, Nb, Cr, Ni, Co, Cu, Hf, 10 for FeO, MgO, K_2O and LOI, 15 for CaO, 50 for TiO_2 and 100 for MnO and P_2O_5.

$(OH)_4$, is known to deviate markedly from the ideal composition by substitution of:

(i) $(Mg, Fe^{2+})^{VI} + Si^{IV} \Leftrightarrow Al^{VI} + Al^{IV}$ (tschermakitic or phengitic substitution; Guidotti, 1984; Massonne and Schreyer, 1987; Guidotti and Sassi, 1998)
(ii) $Fe^{3+} \Leftrightarrow Al^{VI}$ (ferrimuscovite substitution; Guidotti and Sassi, 1998)
(iii) $Na \Leftrightarrow K$ (paragonitic substitution; Guidotti and Sassi, 1998)
(iv) $(Na, K) + Si \Leftrightarrow Ca + Al$ (margaritic substitution; Guidotti and Sassi, 1998)

In order to assess the compositional variation of white-mica as a function of strain, chemical analyses of samples from Types A, B and C are plotted in Fig. 8, which include micas from the matrix and quarter mats.

According to the Si vs Al_{tot} content (Fig. 8a), the three fabric types define well-marked fields, with a higher phengitic content associated with rocks of the highest strain evidence (Si from average values of 6.08 a.p.f.u. in Type A, 6.19 a.p.f.u. in Type B, to 6.61 a.p.f.u. in Type C). The paragonitic content ($Na/(Ca+Na+K)$) also shows a variation with respect to mylonite type (Fig. 8b), with a decrease in this parameter from micas of Type A (=0.6–0.4) to B (=0.2–0.0) and C (≈ 0.0). HR–TEM examination and selected area electron X-ray diffraction (SAED) pattern of samples with a higher paragonitic content allow the identification of fine intergrowths of muscovite (10 Å fringes) and discrete (≤ 0.1 μm width) paragonite (9.6 Å fringes) packets, probably as a consequence of mechanical interlayering during deformation (Fig. 9). These intergrowths, frequently observed in low-grade metapelites (Frey and Robinson, 1991), explain the paragonitic content measured by EMPA in the micas from Type A. A very low margaritic content ($Ca/(Ca+Na+K) < 0.06$) characterizes all mylonite types.

Guidotti (1984) suggests that in metamorphic rocks, substitution (ii) does not occur by itself, but is accompanied by an even greater amount of substitution (i). If substitutions (i) and (ii) occur together, the process is referred to as 'celadonite' substitution (Guidotti, 1984). Unfortunately, distinction between (i) and (ii) substitutions requires distinguishing between Fe^{2+} and Fe^{3+}, which cannot be done by the electron probe analysis. However, the Fe_{total} behaviour suggests the existence of Fe^{3+} in the white-mica, because the ideal substitution between muscovite–phengite did not occur, and white-mica plots according to the 'celadonite' substitution (Fig. 8c). The more phengitic micas of Type C are also the richest in Fe. Additionally, considering the coexistence of white-mica with magnetite and/or hematite (fO_2 buffers), as in the case of Type C mylonites, for a given *P–T*, the white-mica could contain the maximum amount of Fe^{3+} possible (Guidotti, 1984), and the 'celadonitic' substitution could be effective. The good correlation observed between the $\Sigma(Fe+Mg+Mn)$ value

and Al^{VI} (Fig. 8d) confirms, according to substitution (ii), the presence of Fe^{3+} in the composition of the white-micas. Marked $\Sigma(Fe+Mg+Mn)$ variations can be observed between the three mylonite types (Fig. 8c and d). White-mica from Type A are those with the lowest $\Sigma(Fe+Mg+Mn)$ content (<0.2) with $Fe/(Fe+Mg) > 0.7$. White-mica from Type B present $\Sigma(Fe+Mg+Mn)$ values between 0.2 and 1.0 and $Fe/(Fe+Mg) \approx 0.5$. Type C presents the highest values of $\Sigma(Fe+Mg+Mn)$, from 0.7 to 1.5, with $Fe/(Fe+Mg) \approx 0.5$.

No major differences were observed in the chemistry of the micas with respect to their recrystallization domain (matrix vs quarter mats) (Fig. 8). Only micas of Type B show a slight chemical correlation with respect to their structural domain, with a higher $\Sigma(Fe+Mg+Mn)$ in those developed within quarter mats (Fig. 8d).

6. Controls on white-mica composition

It is well known that white-mica composition depends on physical (temperature, confining pressure) and chemical (whole rock and fluids) conditions. Strain conditions would also play a role in low-grade ignimbritic mylonites. In fact, all of these variables must be taken into account in order to explain the chemical variability observed in the white-mica composition of the SGSZ.

6.1. Temperature and pressure

Guidotti (1984) suggests that the $Na/(Ca+Na+K)$ ratio (paragonitic content) increases with temperature and H_2O content, independent of the confining pressure and whole-rock composition. In the low-grade mylonites, white-mica with a paragonitic content is present in Types A and B (Fig. 4b). These low-grade temperatures are consistent with those suggested by fluid-assisted deformation mechanisms and strain softening. In consequence, a relatively homogeneous deformation temperature (low-grade) is proposed for all mylonite types. Thus, the white-mica content of paragonite is not significantly controlled by a temperature variation between the three different mylonite fabric types but corresponds to fine mechanical interlayering of discrete packages of muscovite and paragonite as observed by HR-TEM (Fig. 9).

Experimental data from Velde (1965) indicate that the increase in the phengitic and 'celadonitic' components of white-mica is mainly controlled by pressure conditions, and not by bulk composition. This increase results from the substitution between silica and aluminium according to a tschermakitic or phengitic substitution (i). Two balanced reactions have been proposed for the phengite formation (Essene, 1989):

(a) Phengite = K-feldspar + chlorite + quartz + water
(b) Phengite = K-feldspar + phlogopite + quartz + water

Experimental data for reaction (a) were provided by

Table 5
EMPA and EDX analyses of white-mica of Type A, B and C mylonites from the SGSZ

Sample	B115	B115	B115	B115	B115	B115	B115	B115	B115	B115	98GA1	98GA1
Domain	QM	QM	QM	QM	QM	QM	QM	QM	Matrix	Matrix	QM	QM
Type	A	A	A	A	A	A	A	A	A	A	B	B
Analyses	EMPA	EMPA	EMPA	EMPA	EMPA	EMPA	EDX	EDX	EDX	EDX	EMPA	EMPA
SiO_2	47.00	46.05	45.61	47.13	45.43	45.66	46.86	45.75	48.36	46.77	47.30	46.17
TiO_2	0.14	0.14	0.17	0.14	0.22	0.17	0.63	0.35	0.33	0.22	0.15	0.21
Al_2O_3	38.12	37.19	37.14	39.30	37.59	36.52	37.44	37.16	35.33	37.17	37.95	35.49
FeO	0.87	1.06	0.95	0.79	1.02	1.10	0.75	1.08	1.52	1.22	1.42	1.67
MnO	0.00	0.00	0.00	0.00	0.03	0.00	0.00	0.03	0.11	0.02	0.04	0.00
MgO	0.22	0.25	0.21	0.20	0.23	0.26	0.04	0.00	0.03	0.00	0.34	0.41
CaO	0.57	0.41	0.42	0.57	0.61	0.41	0.30	0.18	0.24	0.37	0.64	0.24
Na_2O	2.62	3.53	2.43	4.22	3.41	2.61	2.92	1.78	2.90	2.63	2.19	1.33
K_2O	5.19	4.86	5.75	3.63	4.29	5.54	5.56	6.84	5.25	5.41	6.60	8.18
Total	94.73	93.49	92.69	95.97	92.81	92.27	94.50	93.17	94.07	93.81	96.62	93.70
Si^{4+}	6.114	6.093	6.091	6.031	6.038	6.127	6.122	6.103	6.352	6.157	6.098	6.187
Al^{IV}	1.886	1.907	1.909	1.969	1.962	1.873	1.878	1.897	1.648	1.843	1.902	1.813
Ti^{4+}	0.014	0.014	0.017	0.013	0.022	0.017	0.062	0.035	0.033	0.022	0.014	0.021
Al^{VI}	3.958	3.892	3.938	3.958	3.925	3.903	3.887	3.944	3.821	3.924	3.863	3.793
Fe^{3+}	0.000	0.000	0.000	0.000	0.000	0.000	0.000	0.000	0.000	0.000	0.000	0.000
Cr^{2+}	0.000	0.000	0.000	0.000	0.000	0.000	0.013	0.000	0.000	0.008	0.000	0.000
Fe^{2+}	0.095	0.118	0.106	0.085	0.113	0.123	0.082	0.120	0.167	0.134	0.153	0.187
Mn^{2+}	0.000	0.000	0.000	0.000	0.003	0.000	0.000	0.003	0.012	0.002	0.004	0.000
Mg^{2+}	0.043	0.049	0.043	0.038	0.045	0.052	0.008	0.000	0.006	0.000	0.065	0.082
Ca^{2+}	0.079	0.058	0.061	0.078	0.087	0.059	0.042	0.026	0.034	0.052	0.089	0.034
Na^+	0.661	0.906	0.629	1.048	0.878	0.678	0.740	0.460	0.738	0.671	0.548	0.346
K^+	0.862	0.821	0.979	0.592	0.727	0.948	0.927	1.164	0.880	0.909	1.086	1.399
Σ cations	13.712	13.857	13.772	13.812	13.799	13.781	13.760	13.753	13.690	13.723	13.822	13.861

Sample	98GA1	98GA1	B110	B110	B110	B110	B111	B111	B111	B110	B110	B110	B110
Domain	QM	QM	QM	QM	QM	QM	QM	QM	QM	matrix	matrix	matrix	matrix
Type	B	B	B	B	B	B	B	B	B	B	B	B	B
Analyses	EMPA	EMPA	EMPA	EMPA	EMPA	EMPA	EDX	EDX	EDX	EMPA	EMPA	EMPA	EMPA
SiO_2	46.09	46.69	45.31	44.99	46.73	46.89	46.45	47.28	48.03	44.49	44.36	45.27	45.50
TiO_2	0.21	0.24	0.25	0.24	0.20	0.25	1.90	1.10	0.55	0.22	0.21	0.21	0.17
Al_2O_3	35.31	35.76	35.25	34.11	35.92	35.01	31.36	32.84	32.96	34.55	33.69	34.74	34.55
FeO	1.80	1.55	2.14	2.13	1.76	2.00	5.23	2.96	3.02	4.11	3.50	3.02	2.50
MnO	0.02	0.02	0.03	0.00	0.01	0.03	0.00	0.00	0.12	0.04	0.05	0.02	0.00
MgO	0.42	0.40	0.45	0.49	0.46	0.46	1.25	0.87	0.88	1.70	1.65	0.97	0.75
CaO	0.18	0.19	0.09	0.11	0.67	0.13	1.30	0.42	0.16	0.16	0.20	0.22	0.29
Na_2O	1.01	0.93	0.72	0.79	1.18	0.87	0.39	0.19	0.15	0.83	0.84	0.90	0.98
K_2O	8.63	8.40	8.69	9.20	7.33	8.72	9.01	9.85	10.80	7.89	7.76	8.42	8.23
Total	93.68	94.17	92.92	92.06	94.27	94.35	96.89	95.51	96.67	93.98	92.27	93.76	92.96
Si^{4+}	6.192	6.213	6.148	6.190	6.195	6.253	6.191	6.303	6.351	6.027	6.099	6.120	6.177
Al^{IV}	1.808	1.787	1.852	1.810	1.805	1.747	1.809	1.697	1.649	1.973	1.901	1.880	1.823
Ti^{4+}	0.021	0.024	0.026	0.025	0.020	0.025	0.190	0.110	0.055	0.023	0.022	0.022	0.018
Al^{VI}	3.783	3.822	3.785	3.721	3.806	3.755	3.117	3.463	3.488	3.543	3.559	3.655	3.705
Fe^{3+}	0.000	0.000	0.000	0.000	0.000	0.000	0.000	0.000	0.000	0.000	0.000	0.000	0.000

Table 5 (*continued*)

Sample	98GA1	98GA1	B110	B110	B110	B110	B111	B111	B111	B110	B110	B110	B110
Domain	QM	QM	QM	QM	QM	QM	QM	QM	QM	matrix	matrix	matrix	matrix
Type	B	B	B	B	B	B	B	B	B	B	B	B	B
Analyses	EMPA	EMPA	EMPA	EMPA	EMPA	EMPA	EDX	EDX	EDX	EMPA	EMPA	EMPA	EMPA
Cr^{2+}	0.000	0.000	0.000	0.000	0.000	0.000	0.009	0.005	0.006	0.000	0.000	0.000	0.000
Fe^{2+}	0.202	0.172	0.243	0.244	0.195	0.223	0.583	0.330	0.334	0.466	0.402	0.341	0.283
Mn^{2+}	0.002	0.002	0.003	0.000	0.001	0.004	0.000	0.000	0.013	0.004	0.006	0.002	0.000
Mg^{2+}	0.085	0.079	0.092	0.101	0.090	0.091	0.248	0.173	0.173	0.343	0.338	0.195	0.152
Ca^{2+}	0.026	0.027	0.013	0.017	0.095	0.018	0.186	0.060	0.023	0.023	0.030	0.032	0.042
Na^{+}	0.264	0.240	0.189	0.209	0.304	0.225	0.101	0.049	0.038	0.217	0.223	0.236	0.258
K^{+}	1.479	1.426	1.503	1.615	1.240	1.483	1.532	1.675	1.822	1.363	1.361	1.452	1.425
Σ cations	13.863	13.792	13.854	13.932	13.752	13.825	13.967	13.866	13.953	13.982	13.942	13.935	13.882

Sample	B110	B110	B110	B110	B110	B110	B110	B110	98GA9	98GA9	98GA9	98GA9	98GA9
Domain	matrix	matrix	matrix	matrix	matrix	matrix	matrix	matrix	QM	QM	QM	QM	QM
Type	B	B	B	B	B	B	B	B	C	C	C	C	C
Analyses	EMPA	EMPA	EMPA	EMPA	EMPA	EMPA	EDX	EDX	EMPA	EMPA	EMPA	EDX	EDX
SiO_2	44.68	45.43	44.53	44.90	43.38	45.17	45.49	49.36	47.67	44.92	44.96	47.92	47.97
TiO_2	0.25	0.15	0.22	0.22	0.24	0.22	0.24	0.35	0.49	0.43	2.42	0.58	0.58
Al_2O_3	34.14	35.59	33.45	33.77	32.68	34.51	34.09	32.5	29.67	26.69	27.76	29.93	24.60
FeO	2.73	2.41	2.59	2.30	5.09	2.60	3.92	2.61	4.77	6.00	6.46	4.67	5.66
MnO	0.01	0.01	0.01	0.01	0.07	0.02	0.00	0.00	0.01	0.00	0.07	0.01	0.00
MgO	0.92	1.01	0.99	0.75	2.35	0.82	1.54	0.49	1.70	1.93	1.89	1.58	3.08
CaO	0.07	0.45	0.11	0.09	0.11	0.08	0.08	0.12	0.10	0.08	0.10	0.00	0.00
Na_2O	0.74	1.35	0.86	0.96	0.65	0.79	0.55	0.27	0.17	0.11	0.20	0.04	0.09
K_2O	8.96	7.27	8.72	8.56	7.20	8.14	8.76	9.26	10.44	10.10	9.46	10.92	10.06
Total	92.49	93.67	91.47	91.57	91.78	92.36	94.67	95.02	95.03	90.27	93.32	95.65	92.04
Si^{4+}	6.134	6.096	6.174	6.198	6.038	6.167	6.125	6.542	6.474	6.493	6.290	6.471	6.759
Al^{IV}	1.866	1.904	1.826	1.802	1.962	1.833	1.875	1.458	1.526	1.507	1.710	1.529	1.241
Ti^{4+}	0.025	0.015	0.023	0.023	0.025	0.022	0.024	0.035	0.050	0.047	0.254	0.059	0.061
Al^{VI}	3.658	3.725	3.639	3.692	3.399	3.718	3.535	3.619	3.222	3.040	2.868	3.235	2.845
Fe^{3+}	0.000	0.000	0.000	0.000	0.000	0.000	0.000	0.000	0.000	0.000	0.000	0.000	0.000
Cr^{2+}	0.000	0.000	0.000	0.000	0.000	0.000	0.001	0.000	0.006	0.000	0.000	0.001	0.000
Fe^{2+}	0.313	0.270	0.300	0.266	0.593	0.297	0.441	0.289	0.542	0.725	0.756	0.527	0.667
Mn^{2+}	0.001	0.001	0.001	0.001	0.008	0.003	0.000	0.000	0.001	0.000	0.009	0.001	0.000
Mg^{2+}	0.188	0.201	0.205	0.155	0.487	0.168	0.309	0.097	0.344	0.416	0.394	0.318	0.647
Ca^{2+}	0.010	0.064	0.016	0.013	0.017	0.012	0.012	0.017	0.015	0.013	0.015	0.000	0.000
Na^{+}	0.198	0.351	0.230	0.257	0.176	0.210	0.144	0.069	0.044	0.031	0.053	0.010	0.025
K^{+}	1.569	1.245	1.542	1.508	1.279	1.417	1.505	1.566	1.809	1.863	1.688	1.881	1.808
Σ cations	13.962	13.872	13.957	13.914	13.984	13.848	13.970	13.699	14.028	14.133	14.038	14.033	14.053

Sample	98GA9	98GA9	98GA9	99GA28A	99GA28A	99GA28A	99GA28A	98GA9	98GA9	98GA9	98GA9	98GA9	98GA9
Domain	QM	QM	QM	QM	matrix	matrix	matrix	matrix	matrix	matrix	matrix	matrix	matrix
Type	C	C	C	C	C	C	C	C	C	C	C	C	C
Analyses	EDX	EDX	EMPA	EMPA	EMPA	EMPA	EMPA	EMPA	EMPA	EMPA	EMPA	EMPA	EMPA
SiO_2	45.65	49.01	47.53	48.57	50.97	46.02	46.24	45.58	46.86	49.01	47.11	45.23	48.57

Table 5 (*continued*)

Sample	98GA9	98GA9	98GA9	99GA28A	99GA28A	99GA28A	99GA28A	98GA9	98GA9	98GA9	98GA9	98GA9	98GA9
Domain	QM	QM	QM	QM	matrix	matrix	matrix	matrix	matrix	matrix	matrix	matrix	matrix
Type	C	C	C	C	C	C	C	C	C	C	C	C	C
Analyses	EDX	EDX	EMPA	EMPA	EMPA	EMPA	EMPA	EMPA	EMPA	EMPA	EMPA	EMPA	EMPA
TiO_2	0.56	0.75	0.24	0.10	0.16	0.13	0.13	0.21	0.27	0.19	0.20	0.09	0.14
Al_2O_3	28.07	27.84	29.26	27.28	24.99	27.75	28.15	28.16	27.93	29.92	29.40	27.21	28.66
FeO	4.78	6.15	5.47	6.33	5.13	5.84	5.40	5.50	5.57	4.71	4.88	5.49	5.68
MnO	0.08	0.00	0.00	0.04	0.07	0.03	0.01	0.04	0.00	0.01	0.03	0.01	0.01
MgO	1.62	1.99	1.92	2.50	1.74	2.11	2.10	2.02	2.25	1.75	1.77	1.74	1.74
CaO	0.00	0.08	0.03	0.21	0.10	0.09	0.07	0.06	0.04	0.06	0.04	0.04	0.01
Na_2O	0.04	0.00	0.29	0.09	0.12	0.08	0.09	0.13	0.19	0.12	0.14	0.16	0.11
K_2O	9.96	9.19	10.36	9.55	10.29	9.45	8.99	10.44	10.61	11.06	10.56	10.89	11.31
Total	90.76	95.01	95.09	94.67	93.56	91.50	91.18	92.15	93.71	96.83	94.12	90.85	96.22
Si^{4+}	6.494	6.638	6.475	6.638	7.005	6.509	6.521	6.437	6.504	6.536	6.472	6.503	6.568
Al^{IV}	1.506	1.362	1.525	1.362	0.995	1.491	1.479	1.563	1.496	1.464	1.528	1.497	1.432
Ti^{4+}	0.060	0.076	0.024	0.010	0.016	0.014	0.014	0.023	0.028	0.019	0.020	0.009	0.014
Al^{VI}	3.199	3.083	3.173	3.032	3.052	3.134	3.201	3.126	3.073	3.237	3.231	3.114	3.136
Fe^{3+}	0.000	0.000	0.000	0.000	0.000	0.000	0.000	0.000	0.000	0.000	0.000	0.000	0.000
Cr^{2+}	0.002	0.000	0.000	0.000	0.000	0.000	0.000	0.000	0.000	0.000	0.000	0.000	0.000
Fe^{2+}	0.569	0.697	0.623	0.723	0.590	0.690	0.636	0.649	0.647	0.525	0.561	0.660	0.643
Mn^{2+}	0.010	0.000	0.000	0.004	0.008	0.003	0.002	0.005	0.000	0.001	0.003	0.001	0.001
Mg^{2+}	0.344	0.402	0.389	0.509	0.357	0.446	0.441	0.426	0.465	0.347	0.363	0.372	0.350
Ca^{2+}	0.000	0.012	0.005	0.030	0.015	0.014	0.011	0.010	0.006	0.009	0.006	0.006	0.001
Na^+	0.011	0.000	0.076	0.025	0.031	0.021	0.024	0.035	0.051	0.031	0.037	0.044	0.028
K^+	1.807	1.588	1.800	1.664	1.804	1.706	1.618	1.881	1.879	1.882	1.851	1.997	1.951
Σ cations	14.002	13.857	14.090	13.999	13.873	14.028	13.946	14.154	14.148	14.051	14.072	14.203	14.123

Sample	98GA9	98GA9	98GA9	98GA9	98GA9	98GA9	98GA9	98GA9	98GA9
Domain	matrix	matrix	matrix	matrix	matrix	matrix	matrix	matrix	matrix
Type	C	C	C	C	C	C	C	C	C
Analyses	EMPA	EMPA	EMPA	EMPA	EMPA	EDX	EDX	EDX	EDX
SiO_2	50.17	54.23	46.72	51.34	48.05	46.21	46.73	53.98	51.37
TiO_2	0.07	0.70	0.47	0.61	0.24	0.66	0.46	0.13	0.13
Al_2O_3	27.81	26.57	29.86	26.01	28.94	25.60	27.80	26.59	28.53
FeO	4.76	4.94	4.28	4.76	4.38	5.37	9.13	3.38	3.94
MnO	0.00	0.02	0.01	0.00	0.01	0.00	0.00	0.00	0.01
MgO	2.20	2.15	1.84	1.77	1.72	2.18	2.31	1.68	1.92
CaO	0.03	0.07	0.06	0.06	0.08	0.00	0.02	0.10	0.02
Na_2O	0.05	0.12	0.17	0.10	0.12	0.18	0.13	0.10	0.02
K_2O	10.75	9.24	10.30	9.72	9.99	9.91	10.47	11.85	9.93
Total	95.85	98.03	93.69	94.36	93.54	90.11	97.19	97.81	95.87
Si^{4+}	6.738	7.022	6.422	6.949	6.589	6.649	6.371	7.054	6.812
Al^{IV}	1.262	0.978	1.578	1.051	1.411	1.351	1.629	0.946	1.188
Ti^{4+}	0.007	0.068	0.048	0.062	0.025	0.071	0.047	0.013	0.013
Al^{VI}	3.140	3.076	3.259	3.097	3.266	2.990	2.838	3.149	3.270
Fe^{3+}	0.000	0.000	0.000	0.000	0.000	0.000	0.000	0.000	0.000
Cr^{2+}	0.000	0.000	0.000	0.000	0.000	0.000	0.015	0.009	0.000
Fe^{2+}	0.534	0.535	0.492	0.538	0.502	0.646	1.041	0.369	0.437

Table 5 (continued)

Sample	98GA9	98GA9	98GA9	98GA9	98GA9	98GA9	98GA9	98GA9	98GA9
Domain	matrix	matrix	matrix	matrix	matrix	matrix	matrix	matrix	matrix
Type	C	C	C	C	C	C	C	C	C
Analyses	EMPA	EMPA	EMPA	EMPA	EMPA	EDX	EDX	EDX	EDX
Mn^{2+}	0.000	0.002	0.001	0.000	0.001	0.000	0.000	0.000	0.001
Mg^{2+}	0.440	0.414	0.377	0.358	0.351	0.468	0.469	0.327	0.380
Ca^{2+}	0.005	0.010	0.008	0.008	0.012	0.000	0.003	0.014	0.003
Na^+	0.013	0.031	0.046	0.026	0.033	0.050	0.034	0.025	0.005
K^+	1.842	1.526	1.806	1.678	1.748	1.819	1.821	1.975	1.680
Σ cations	13.982	13.662	14.037	13.767	13.938	14.044	14.269	13.882	13.789

The structural formulae was calculated on the basis of 22 oxygens. Total Fe was calculated as FeO.

Massonne and Schreyer (1987), Bucher-Nurminen (1987) and Massonne and Szpurka (1997), obtaining a calibration for the pressure estimation. The most important control for the application of the barometer proposed is the presence of the buffering phase K-feldspar under equilibrium conditions (Essene, 1989). In the absence of K-feldspar the phengite barometry provides only a minimum estimate of pressure. The pressure obtained by this method for the highest Si content in white-mica coexisting with a biotite-K feldspar assemblage (Type C) ranges from 2.0 to 7.5 kbar, for the 350–400 °C temperature range. The minimum pressure for Type A and B mylonites is estimated between 1.0 and 5.0 kbar (Arancibia, 2002, 2004).

Etheridge (1983) showed that differential stress in shear zones is mainly of the order of 0.1–0.2 kbar, and is negligible in comparison with the lithostatic pressure. Thus, although deformation resulting from differential stresses plays a major role in determining the microstructural characteristics of rocks, it does not influence the mineral assemblage which, in turn, is controlled by the lithostatic pressure. Moreover, during the deformation processes, reaction catalysis and/or fluid movement would be favoured (Yardley, 1990). If a fluid phase is present, the fluid pressure tends to act in the opposite sense to the applied stress, reducing the effective confining pressure. Therefore, the maximum possible pressure estimation for any shear zone corresponds to the lithostatic pressure. For the SGSZ mylonites, pressures of the order of 7.5 kbar are unlikely. Low-pressure conditions below 3 kbar for the non-deformative regional very-low grade metamorphism of the Triassic ignimbrites (= protolith) were proposed by Oyarzún et al. (1997). This figure could be considered as the upper limit of the confining pressure and is consistent with a normal P–T gradient regime for brittle–ductile transition conditions estimated for the SGSZ. Thus, the phengitic–celadonitic component in the white-mica does not appear to be related to lithostatic pressure influence (Arancibia, 2004).

6.2. Whole-rock vs fluid composition

According to the microstructure developed in these mylonites, low-temperature conditions for the mylonitic deformation can be assumed. The felsic nature of the protolith together with the low-temperature conditions only permit a reduced low-variance spectrum of possible metamorphic minerals, with white-mica, chlorite, plagioclase and quartz and minor K-feldspar, biotite and opaque minerals as the dominant metamorphic mineral phases. This mineralogy is consistent with a low-alumina KFMASH (+Na) system in which white-mica coexists with feldspars without aluminosilicates such as kaolinite or pyrophyllite (Guidotti and Sassi, 1998) (Fig. 10).

Whole-rock geochemical control on white-mica composition is demonstrated in the $Al_2O_3:Na_2O:K_2O$ triangular diagram (Fig. 10), in which consistency between the white-mica composition and the whole-rock chemistry is observed. A change in the chemistry of the mylonites is clearly observed
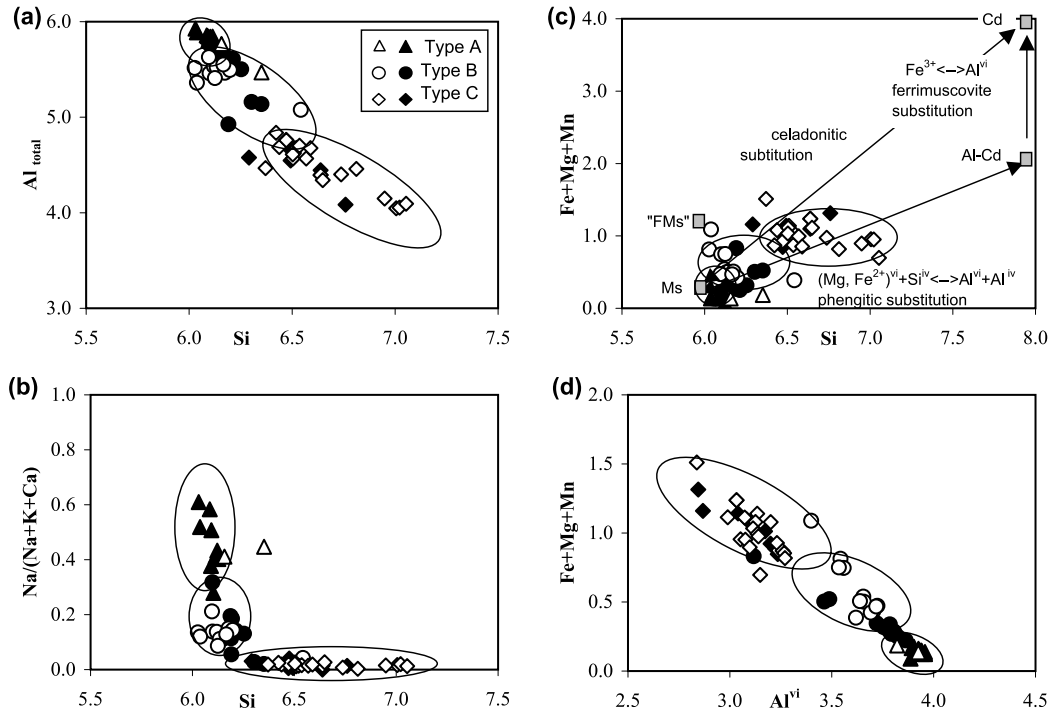
Fig. 8. Composition of white-mica (EMPA and SEM-EDX data in a.p.f.u.) of the three fabrics of mylonites from the SGSZ. Open symbols indicate white-mica from the matrix and full symbols white-mica from the quarter mat (QM) structures. (a) Si vs Al_{total} for white-micas from the SGSZ mylonites. (b) Si vs $Na/(Na+K+Ca)$ (paragonitic substitution) for white-micas from the SGSZ mylonites. (c) Si vs $\Sigma(Fe_T+Mg+Mn)$ for white-micas from the SGSZ mylonites. The ideal compositions of muscovite (Ms), 'ferrimuscovite' (FMs), phengite (Phe) and ferriphengite (Fphe), celadonite (Cd) and aluminoceladonite (Al-Cd) taken from Guidotti and Sassi (1998), are shown by lightly shaded squares. The white-micas of the SGSZ plot according to the celadonitic substitution. (d) Al^{VI} vs $\Sigma(Fe_T+Mg+Mn)$ for white-micas from the SGSZ mylonites, showing a good correlation interpreted to derive from the presence of Fe^{3+} in the chemical composition of these micas. See text for details.

from Type A (plotting close to the protolith composition) to Type C. In this sense, K-rich mylonites (Type C) have the highest K content in white-micas with presence of fine-grained KFd in the matrix and/or fractures (Figs. 8 and 10; Tables 4 and 5). A higher paragonitic component (presence of a fine intergrowth of discrete paragonite–muscovite) in micas developed in the mylonites of Type A is consistent with the
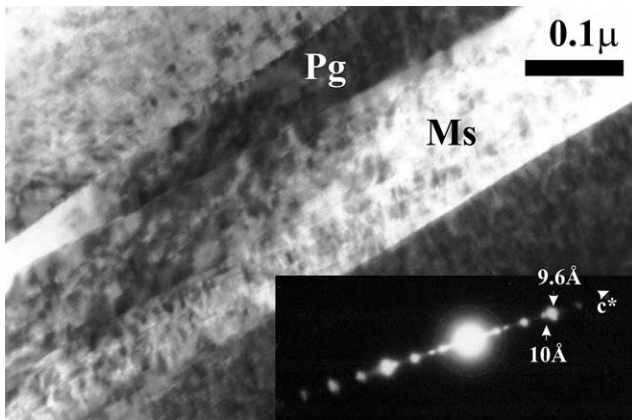
Fig. 9. Low-magnification HR-TEM image of white-mica quarter mats from sample B-115 (mylonite of Type A) showing fine paragonite (Pg)-muscovite (Ms) interlayering. The SAED pattern (inset) shows the 10 Å (Ms) and 9.6 Å (Pg) periodicities indicating the Ms–Pg interlayering.

whole-rock composition (Fig. 10). On the other hand, in spite of the inherent heterogeneity of the ignimbritic protolith, the high K content observed in mylonites of Type C has been previously shown to be related to a secondary metasomatic event during deformation. Consequently, the high K-content of the whole-rock favours the high K-content in the white-mica (phengitic composition) of these mylonites. Finally, high fO_2 conditions deduced from the high Fe_2O_3/FeO ratio observed in Type C mylonites (Fig. 5f) favour the increased proportion of iron oxides observed in these mylonites with respect to the other mylonite types.

6.3. Strain and white-mica generation

Microstructures developed in the low-grade SGSZ mylonites suggest similar deformational mechanisms in the three mylonite types at similar temperature conditions. Minor cataclasis of feldspar and quartz followed by important reaction-enhanced softening involving the production of phyllosilicates from dissolved quartz and feldspar porphyroclast, are determined to be the main mechanisms by which the three different types of mylonites are formed. These processes may explain the well-oriented mica and chlorite generation in the matrix and quarter mat-strain shadow structures, and relatively well-preserved porphyroclast, during ductile deformation. Differences in the resultant fabrics
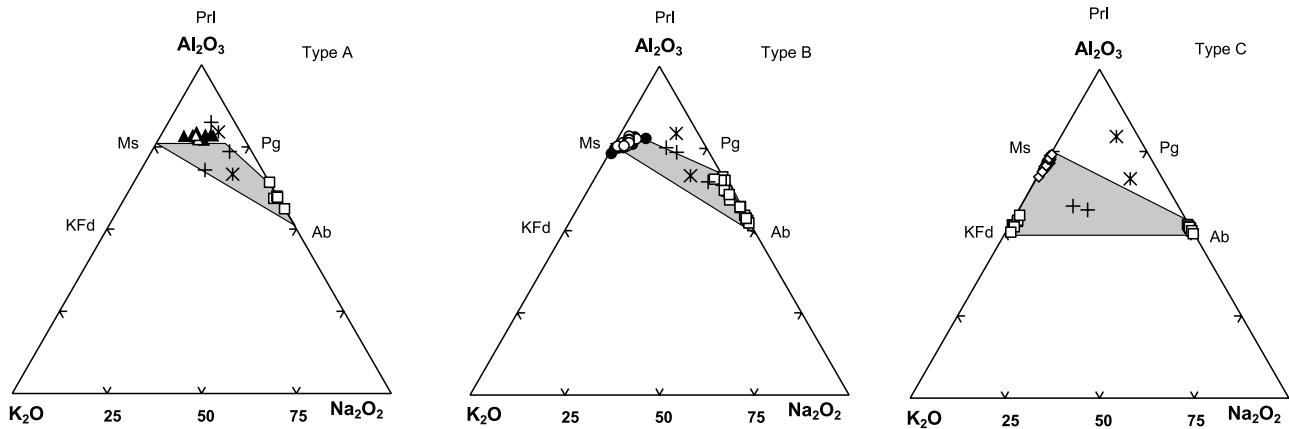
Fig. 10. Projection of whole-rock geochemistry and white-mica composition on the Al_2O_3:K_2O:Na_2O (AKNa) triangular diagram (in molar proportions), according to Guidotti and Sassi (1998), for the SGSZ. Open symbols indicate white-micas from the matrix and full symbols white-micas from the quarter mat (QM) structures. In a high-aluminium system, metamorphic minerals would plot on the Prl:Ms:Pg subtriangle. In a low-aluminium system, the probable metamorphic paragenesis would be Ms+Pg+Ab, Ms+Ab and KFd+Ms+Ab. In all three types, whole-rock (crosses) analyses plot in the tie-line space (shadowed area) defined by the secondary mineral composition. The protolith composition is plotted in the three triangles as stars. Prl, Pyrophyllite; Ms, Muscovite; Pg, Paragonite; KFd, K-feldspar; Ab, Albite.

between the mylonites of the SGSZ would then be attributed to the relative intensity of reaction-softening processes (increasing with strain) reflected in the different proportions of phyllosilicates.

Some differences have been shown mostly in mylonites of Type C with respect to the other two types: a higher white-mica content, weak quarter-mat and strain shadow structure development, higher intracrystalline deformation in porphyroclasts and the development of later extensional crenulation cleavage. In addition, the anomalously high K-content and high Fe^{3+}/Fe^{2+} ratio shown by the whole-rock geochemistry of these Type C mylonites would be explained if a higher fluid/rock interaction ratio operated during the development of this type of mylonite. A higher fluid/rock ratio would be a consequence of the highest strain conditions and would favour the input of K^+ to the system, increasing its fO_2.

Wibberley (1999) concluded that the effect of muscovitization in fault zones is a complex process which is controlled by the permeability, silica solubility and deformational mechanism. In the SGSZ, mylonites with the highest white-mica content (Type C) also show evidence of the highest strain conditions. An evolution of progressive strain from mylonites of Type A to mylonites of Type C could be proposed from the microstructural study. In Type A, deformation is characterized by the recrystallisation of phyllosilicates in the matrix and the main mechanism of deformation would be dissolution and phyllosilicate precipitation. Deformation would continue together with an increase in the white-mica content and decrease in the porosity, allowing strain location around porphyroclasts and consequently pressure shadow and quarter mat structure development by remobilization of the previously generated fine-grained phyllosilicates (mylonites of Type B). During this stage, the white-mica would increase in content and size. Finally, with an increase in strain, more intense intracrystalline deformation

would be observed in porphyroclasts and quarter mats and pressure-shadows would be obliterated (Type C). White-mica generation would be favoured, reaching their highest proportions. The whole deformational process is characterized by low-variance neoformed paragenesis, in which the white-mica composition would be controlled by the whole-rock chemistry and related to the strain conditions as previously discussed.

7. Conclusions

The SGSZ in the Coastal Range of central Chile affects ignimbrites of the Triassic Pichidangui Formation. Three different fabrics can be established according to the mylonitic microstructure. Types A, B and C represent mylonites with evidence of relatively low, intermediate, and high strain, respectively. The main deformational mechanisms operating during ductile deformation were cataclasis and dissolution of feldspar and quartz crystals, followed by reaction softening processes with phyllosilicate generation. All these mechanisms favour the orientation of phyllosilicates (white-mica and chlorite) in the matrix together with quarter mat and strain shadow structures; porphyroclasts would be relatively well preserved. Deformation mechanisms suggest low-temperature (350–400 °C) conditions of mylonitic deformation in the presence of fluids, with the development of low-variance paragenesis. These conditions are consistent with the temperature estimation based on chlorite chemistry. The geological setting of the SGSZ suggests low-pressure (<3 kbar) conditions.

The composition of white-mica from the three different fabrics shows a clear correlation between chemistry and strain intensity. The highly strained mylonites (Type C) contain the highest phengitic–celadonitic micas, whereas low-strain

mylonites (Type A) have the largest proportion of paragonitic, non-phengitic micas. White-micas from Type B mylonites show composition intermediate between those of Types A and C. Application of a geobarometer based on the white-mica composition in highly deformed rocks yields pressure values with no geological significance in our case. This could be explained by the anomalously high K metasomatic input during ductile deformation of highly strained rocks, controlling the white-mica composition. For mylonites of Types A and B, minor differences in the white-mica chemical composition is mostly controlled by small differences in whole-rock composition and strain, with the Na-rich white-mica occurring in the Na_2O richer mylonite of Type A. According to our results, in the SGSZ a high K ($=$phengitic) content in white-mica from the most intensively strained mylonite (Type C) is not related to high-pressure conditions during deformation. A high Na ($=$paragonitic) content in white-mica from the least-strained mylonites (Type A) are not related to a significant increase in temperature. In conclusion, the whole-rock geochemistry together with differences in strain must be considered to understand the white-mica composition of low-grade mylonites.

Acknowledgements

References

Arancibia, G. 2002. Geometría, cinemática condiciones y edad de la deformación milonítica en rocas volcánicas. El caso de la Zona de Falla Silla del Gobernador, Chile central (32°S). Unpublished PhD thesis, Universidad de Chile.

Arancibia, G., 2004. Mid-Cretaceous crustal shortening: evidence from a regional-scale ductile shear zone in the Coastal Range of central Chile (32° Lat. S). Journal of South American Earth Sciences 17, 209–226.

Berthé, D., Choukroune, P., Jegouzo, P., 1979. Orthogneiss, mylonite and non-coaxial deformation of granites: the example of the South Armorican shear zone. Journal of Structural Geology 1, 31–42.

Bialek, D., 1999. Chemical changes associated with deformation of granites under greenschist facies conditions: the example of the Zawidow Granodiorite (SE Lusatian Granodiorite Complex, Poland). Tectonophysics 303, 251–261.

Bos, B., Spiers, C., 2001. Experimental investigation into the microstructural and mechanical evolution of phyllosilicates-bearing fault rocks under favouring pressure solution. Journal of Structural Geology 23, 1187–1202.

Bucher-Nurminen, K., 1987. A recalibration of the chlorite–biotite–muscovite geobarometer. Contributions to Mineralogy and Petrology 96, 519–522.

Cathelineau, M., 1988. Cation site occupancy in chlorites and illites as a function of temperature. Clay Minerals 23, 471–485.

Charrier, R., Godoy, E., Bertens, A., Larranguibel, J., 1991. La Falla de La Silla del Gobernador, Quilimarí, región de Coquimbo, Chile: Antecedentes cinemáticos y significado geológico. In: VI Congreso Geológico Chileno, Viña del Mar, pp. 548–555.

Condie, K.C., Sinha, A.K., 1996. Rare earth and other trace element mobility during mylonitization: a comparison of the Brevard and Hope Valley shear zones in the Appalachian Mountains, USA. Journal of Metamorphic Geology 14, 213–226.

Conti, P., Funedda, A., Cerbai, N., 1998. Mylonite development in the Hercynian basement of Sardinia (Italy). Journal of Structural Geology 20, 121–133.

Essene, E.J., 1989. The current status of thermobarometry in metamorphic rocks. In: Daly, J., Cliff, R., Yardley, B. (Eds.), Evolution of Metamorphic Belts. Geological Society Special Publication, 43, pp. 1–44.

Etheridge, M.A., 1983. Differential stress magnitudes during regional metamorphism: upper bound imposed by tensile fracturing. Geology 11, 231–234.

Evans, J.P., 1990. Textures, deformation mechanism, and the role of fluids in the cataclastic deformation of granitic rocks. In: Knipe, R., Rutter, E. (Eds.), Deformation mechanisms, Rheology and Tectonics. Geological Society Special Publication, 54, pp. 29–39.

Fitz Gerald, J., Stünitz, H., 1993. Deformation of granitoids at low metamorphic grade. I: reactions and grain size reduction. Tectonophysics 221, 269–297.

Frey, M., Robinson, D. (Eds.), 1991. Low-Grade Metamorphism. Blackwell Science, 313pp.

Grant, J.A., 1986. The isocon diagram—a simple solution to Gresens' equation for metasomatic alteration. Economic Geology 81, 1976–1982.

Groshong, R., 1988. Low-temperature deformation mechanisms and their interpretation. Geological Society of America Bulletin 100, 1329–1360.

Guidotti, C.V., 1984. Micas in metamorphic rocks. In: Bailey, S.W. (Ed.), Micas Reviews in Mineralogy, 13, pp. 357–467.

Guidotti, C., Sassi, F., 1998. Petrogenetic significance of Na–K white mica mineralogy: recent advances for metamorphic rocks. European Journal of Mineralogy 10, 815–854.

Handy, M., 1990. The solid-state flow of polymineralic rocks. Journal of Geophysical Research 95, 8647–8661.

Hanmer, S., Passchier, C., 1991. Shear-sense indicators: a review. Geological Survey of Canada, Paper 90–17, 72pp.

Hippertt, J.F., 1994. Microstructures and c-axis fabrics indicative of quartz dissolution in sheared quartzites and phyllonites. Tectonophysics 229, 141–163.

Hippertt, J.F., 1998. Breakdown of feldspar, volume gain and lateral mass transfer during mylonitization of granitoid in a low metamorphic grade shear zone. Journal of Structural Geology 20, 175–193.

Knipe, R., 1989. Deformation mechanism-recognition from natural tectonites. Journal of Structural Geology 11, 127–146.

Leat, P., Schmincke, H., 1993. Large-scale rheomorphic shear deformation in Miocene peralkaline ignimbrite E, Gran Canaria. Bulletin of Volcanology 55, 155–165.

Massonne, H.J., Schreyer, W., 1987. Phengite geobarometry based on the limiting assemblage with K-feldspar, phlogopite and quartz. Contributions to Mineralogy and Petrology 96, 212–224.

Massonne, H.J., Szpurka, Z., 1997. Thermodynamic properties of white micas on the basis of high-pressure experiments in the systems K_2O–MgO–Al_2O_3–SiO_2–H_2O and K_2O–FeO–Al_2O_3–SiO_2–H_2O. Lithos 41, 229–250.

Mitra, G., 1984. Brittle to ductile transition due to large strains along the White Rock Thrust. Wind River mountains, Wyoming. Journal of Structural Geology 6, 51–61.

Morata, D., Aguirre, L., Oyarzún, M., Vergara, M., 2000. Crustal contribution in the genesis of the bimodal Triassic volcanism from the Coastal Range, central Chile. Revista Geológica de Chile 27, 83–98.

O'Hara, K., 1988. Fluid flow and volume loss during mylonitization: an origin for phyllonite in an overthrust setting, North Carolina, USA. Tectonophysics 156, 21–36.

Oyarzún, M., Aguirre, L. Morata, D., 1997. Quimismo bimodal y metamorfismo de bajo grado en las rocas volcánicas triásicas de la Cordillera de la Costa de Chile central. In: VIII Congreso Geológico Chileno, Universidad Católica del Norte (eds.), II, pp. 1424–1428, Antofagasta, Chile.

Passchier, C., Simpson, C., 1986. Porphyroclast systems as kinematics indicators. Journal of Structural Geology 8, 831–843.

Passchier, C., Trouw, R. (Eds.), 1996. Micro-tectonics. Springer-Verlag, Berlin, Heidelberg, Germany, 289pp.

Platt, J.P., Vissers, R., 1980. Extensional structures in anisotropic rocks. Journal of Structural Geology 2, 397–410.

Potdevin, J.L., 1993. Gresens 92: a simple Macintosh program of the Gresens method. Computer and Geosciences 19, 1229–1238.

Pryer, L., 1993. Microstructures in feldspar from a major crustal thrust zone: the Grenville Front, Ontario, Canada. Journal of Structural Geology 15, 21–36.

Ruiz-Cruz, M.D., 1999. New data for metamorphic vermiculite. European Journal of Mineralogist 11, 533–548.

Rutter, E.H., 1983. Pressure solution in nature, theory and experiment. Journal of the Geological Society of London 140, 725–740.

Sassie, F.P., Scolari, A., 1974. The b_o value of the potassic white mica as a barometric indicator in low grade metamorphism of pelitic schist. Contributions to Mineralogy and Petrology 45, 143–152.

Shea, W., Kronenberg, A., 1992. Rheology and deformation mechanisms of an isotropic mica schist. Journal of Geophysical Research 97, 15201–15237.

Spear, F.S. 1993. Metamorphic Phase Equilibria and Pressure–Temperature–Time Paths. Mineralogical Society of America Monograph, Washington, DC.

Tullis, J., Yund, R., 1985. Dynamic recrystallisation of feldspar: a mechanism from ductile shear zone formation. Geology 13, 238–241.

Tullis, T., Wood, D., 1975. Correlation of finite strain from both reduction bodies and preferred orientation of mica in slate from Wales. Bulletin of Geological Society of America 86, 632–638.

Van Staal, C.R., Rogers, N., Taylor, B., 2001. Formation of low-temperature mylonites and phyllonites by alkali-metasomatic weakening of felsic volcanic rocks during progressive, subduction-related deformation. Journal of Structural Geology 23, 903–921.

Velde, B., 1965. Phengite micas: synthesis, stability and natural occurrence. American Journal of Science 263, 886–913.

Velde, B., 1978. High temperature of metamorphic vermiculites. Contributions to Mineralogy and Petrology 66, 319–323.

White, S.H., Knipe, R.J., 1978. Transformation- and reaction-enhanced ductility in rocks. Journal of Geological Society of London 135, 513–516.

White, S., Burrows, S., Carreras, J., Shaw, N., Humphreys, F., 1980. On mylonites in ductile shear zones. Journal of Structural Geology 21, 175–187.

Wibberley, C., 1999. Are feldspar-to-mica reactions necessarily reaction-softening processes in fault zones? Journal of Structural Geology 21, 1219–1227.

Williams, M., Burr, J., 1994. Preservation and evolution of quartz phenocryst in deformed rhyolites from the Proterozoic of southwestern North America. Journal of Structural Geology 16, 203–221.

Wintsch, R., 1978. A chemical approach to the preferred orientation of mica. Geological Society of America Bulletin 89, 1715–1718.

Wintsch, R., Christoffersen, R., Kronenberg, A., 1995. Fluid-rock reaction weakening of fault zones. Journal of Geophysical Research 100, 13021–13032.

Yardley, B., 1990. An Introduction to Metamorphic Petrology. Longman Earth Science Series, England p. 248.

Zulauf, G., Palm, S., Petschick, R., 1999. Element mobility and volumetric strain in brittle and brittle-viscous shear zones of the superdeep well KTB (Germany). Chemical Geology 156, 135–149.